

# **Development of AIM-based Fast Solver for Efficient Design and Synthesis of Negative Index Materials**

**AFOSR/AOARD Project Report**

**Grant Number: FA-4868-06-01-0054  
Project Number: AOARD-06-4031  
PI: Professor Joshua Le-Wei Li**

Department of Electrical & Computer Engineering  
National University of Singapore  
10 Kent Ridge Crescent  
Singapore 119260

Report Documentation Page				Form Approved OMB No. 0704-0188	
Public reporting burden for the collection of information is estimated to average 1 hour per response, including the time for reviewing instructions, searching existing data sources, gathering and maintaining the data needed, and completing and reviewing the collection of information. Send comments regarding this burden estimate or any other aspect of this collection of information, including suggestions for reducing this burden, to Washington Headquarters Services, Directorate for Information Operations and Reports, 1215 Jefferson Davis Highway, Suite 1204, Arlington VA 22202-4302. Respondents should be aware that notwithstanding any other provision of law, no person shall be subject to a penalty for failing to comply with a collection of information if it does not display a currently valid OMB control number.					
1. REPORT DATE <b>06 DEC 2007</b>		2. REPORT TYPE <b>Final</b>		3. DATES COVERED <b>09-05-2006 to 03-10-2007</b>	
4. TITLE AND SUBTITLE <b>Development of AIM-Based Fast Solver for Efficient Design and Synthesis of NIMS</b>				5a. CONTRACT NUMBER <b>FA48690610054</b>	
				5b. GRANT NUMBER	
				5c. PROGRAM ELEMENT NUMBER	
6. AUTHOR(S) <b>Joshua Le-Wei Li</b>				5d. PROJECT NUMBER	
				5e. TASK NUMBER	
				5f. WORK UNIT NUMBER	
7. PERFORMING ORGANIZATION NAME(S) AND ADDRESS(ES) <b>National University of Singapore,10 Kent Ridge Crescent,Singapore 119260,Singapore,SG,N/A</b>				8. PERFORMING ORGANIZATION REPORT NUMBER <b>N/A</b>	
9. SPONSORING/MONITORING AGENCY NAME(S) AND ADDRESS(ES) <b>AOARD, UNIT 45002, APO, AP, 96337-5002</b>				10. SPONSOR/MONITOR'S ACRONYM(S) <b>AOARD-064031</b>	
				11. SPONSOR/MONITOR'S REPORT NUMBER(S)	
12. DISTRIBUTION/AVAILABILITY STATEMENT <b>Approved for public release; distribution unlimited</b>					
13. SUPPLEMENTARY NOTES					
14. ABSTRACT <b>This report presents a fast hybrid volume-surface integral equation approach for the computation of electromagnetic scattering from composite left-handed materials (LHM) such as split-ring resonators (SRR) with wires. The volume electric field integral equation (EFIE) is applied to the dielectric region of this LHM, and the surface electric field integral equation is applied on the conducting surface. The method of moments (MoM) is used to discretize the integral equation into a matrix solution and adaptive integral method (AIM) is employed to reduce the memory requirement and CPU time for the matrix solution. This approach is applied to antenna design to improve the performance of an ordinary microstrip-feed patch antenna. The antenna's bandwidth is greatly broadened while the VSWR remains very low and radiation efficiency is high. The future interesting and practical research is also proposed in the report.</b>					
15. SUBJECT TERMS					
16. SECURITY CLASSIFICATION OF:			17. LIMITATION OF ABSTRACT <b>Same as Report (SAR)</b>	18. NUMBER OF PAGES <b>64</b>	19a. NAME OF RESPONSIBLE PERSON
a. REPORT <b>unclassified</b>	b. ABSTRACT <b>unclassified</b>	c. THIS PAGE <b>unclassified</b>			

# Abstract

---

This report presents a fast hybrid volume-surface integral equation approach for the computation of electromagnetic scattering from composite left-handed materials (LHM) such as split-ring resonators (SRR) with wires. The volume electric field integral equation (EFIE) is applied to the dielectric region of this LHM, and the surface electric field integral equation is applied on the conducting surface. The method of moments (MoM) is used to discretize the integral equation into a matrix solution and adaptive integral method (AIM) is employed to reduce the memory requirement and CPU time for the matrix solution. The present approach is sufficiently versatile in handling scattering problems of such composite LHMs, due to the combination of volume and surface electric field integral equations. This algorithm is first verified in a scattering problem of an ordinary composite right-handed material structure. Then we use the algorithm to find the resonance frequency of a few SRRs. In order to demonstrate the accuracy and efficiency of this technique, we present the numerical results of calculating the radar cross section (RCS) of such an SRR slab. Then based on previous knowledge of such structure, we designed a new left-handed structure on microstrip line with capacitor gaps. Simulation results show the backward-wave characteristic of this structure. And then we apply this structure in antenna design to improve the performance of an ordinary microstrip-feed patch antenna. The antenna's bandwidth is greatly broadened while the VSWR remains very low and radiation efficiency is high. In the end, some future research proposals focus on interesting and practical topics are also included in the report.

# Contents

<b>Abstract</b>	<b>i</b>
<b>Contents</b>	<b>ii</b>
<b>List of Figures</b>	<b>iv</b>
<b>1 Introduction</b>	<b>1</b>
<b>2 Split-Ring Resonators and Adaptive Integral Method</b>	<b>5</b>
2.1 Split-Ring Resonators . . . . .	5
2.2 Method of Moments . . . . .	7
2.3 Adaptive Integral Method . . . . .	9
2.3.1 the Advantages of Adaptive Integral Method (AIM) . . . . .	9
2.3.2 Introduction of Hybrid Volume-Surface Integral Equation . . . . .	10
2.3.3 Formulations For Hybrid Volume-Surface Integral Equation . . . . .	10
2.3.4 RWG and SWG basis function . . . . .	11
2.3.5 Formulations for AIM . . . . .	13
<b>3 Numerical Result for AIM</b>	<b>16</b>
3.1 Validation of the VSIE-AIM Algorithm . . . . .	16
3.2 Resonance Frequency of SRRs . . . . .	16
3.2.1 Geometry Statement of SRR structure . . . . .	16
3.2.2 Resonance Frequency of SRRs . . . . .	16
3.3 RCS of a SRR Slab With Different Plane-Waves as Illuminator . . . . .	19
3.4 Conclusion for AIM Algorithm . . . . .	26

<b>4</b>	<b>Application of Left-handed Material with New Designs</b>	<b>27</b>
4.1	Microstrip Lines Loaded With Flower-shaped Left-handed Resonators . . . . .	27
4.1.1	Introduction of Microstrip Lines Loaded with CSRR and Capatitors . . . .	27
4.1.2	The Novel Planar Negative Refractive Index Structure . . . . .	28
4.2	Microstrip-feed Patch Antenna with Left-handed Elements . . . . .	30
4.2.1	Novel Patch Antenna with LH Element and Its Performance . . . . .	30
4.2.2	Conclusion for the Application . . . . .	37
<b>5</b>	<b>Proposed Future Research Topics</b>	<b>40</b>
<b>A</b>	<b>Useful Formulations</b>	<b>43</b>
A.1	RWG Basis Function – Triangular Modeling Method for Surface Element . . . . .	43
A.1.1	Development of RWG Basis Function . . . . .	43
A.1.2	Testing Procedure of RWG Basis Function . . . . .	45
A.1.3	Elements of the Matrix and Excitation Vector of RWG . . . . .	47
A.2	SWG Basis Function – Tetrahedral Modeling Method for Volume Element . . . . .	48
A.2.1	Development of SWG Basis Function . . . . .	48
A.2.2	Testing Procedure of SWG Basis Function . . . . .	51
A.2.3	Elements of the Matrix and Excitation Vector of SWG . . . . .	52

# List of Figures

1.1	Poyntings vector and the wave vector for wave propagations in right-handed and left-handed materials. . . . .	2
1.2	Round and square split-ring resonators . . . . .	2
2.1	Split-rings resonators with rods . . . . .	6
2.2	Split-ring resonators with wires . . . . .	6
2.3	Different combination of $\varepsilon$ and $\mu$ . . . . .	7
2.4	Geometry of scatterer consisting of dielectric material and conducting body embedded in an isotropic homogeneous medium . . . . .	11
3.1	Bistatic RCS of a coated dielectric sphere ( $a_1 = 0.9$ m, $\varepsilon_{r1} = 1.4 - 0.3j$ ; $a_2 = 1$ m, $\varepsilon_{r2} = 1.6 - 0.8j$ ) at 750 MHz. . . . .	17
3.2	The front and back view of 1 SRR inclusion . . . . .	17
3.3	The rings view of 1 row of SRRs (inclusions) . . . . .	18
3.4	The wire view of 1 row of SRRs (inclusions) . . . . .	18
3.5	SCS versus frequency for a row of inclusions (3 SRRs) at $\theta = \phi = 90^\circ$ . . . . .	18
3.6	Structure of the slab composed by SRRs and wires with and two different incidents in the reference frame . . . . .	19
3.7	$E_z$ of the slab of case $< 1 >$ at 15.8 GHz . . . . .	20
3.8	RCS of the slab of case $< 1 >$ at 15.8 GHz . . . . .	20
3.9	$E_z$ of the slab of case $< 2 >$ at 15.8 GHz . . . . .	21
3.10	RCS of the slab of case $< 2 >$ at 15.8 GHz . . . . .	21
3.11	$E_z$ of the slab of case $< 1 >$ at 15.8 GHz when $\varepsilon = 1.60 - 0.05j$ . . . . .	22
3.12	RCS of the slab of case $< 1 >$ at 15.8 GHz when $\varepsilon = 1.60 - 0.05j$ . . . . .	22

3.13	$E_z$ of the slab of case < 2 > at 15.8 GHz when $\varepsilon = 1.60 - 0.05j$ . . . . .	23
3.14	RCS of the slab of case < 2 > at 15.8 GHz when $\varepsilon = 1.60 - 0.05j$ . . . . .	23
3.15	$E_z$ of the slab of case < 1 > at 15.8 GHz when $\varepsilon = 2.40 - 0.20j$ . . . . .	24
3.16	RCS of the slab of case < 1 > at 15.8 GHz when $\varepsilon = 2.40 - 0.20j$ . . . . .	24
3.17	$E_z$ of the slab of case < 2 > at 15.8 GHz when $\varepsilon = 2.40 - 0.20j$ . . . . .	25
3.18	RCS of the slab of case < 2 > at 15.8 GHz when $\varepsilon = 2.40 - 0.20j$ . . . . .	25
4.1	Proposed 2D NRI structure. (a) Upper layer. (b) Lower layer. (c) Unit cell. . . . .	29
4.2	Top view of a microstrip line with 2 rows of triangle-shaped left-handed pattern on the ground plane . . . . .	29
4.3	Top view of a microstrip line with 2 rows of flower-shaped left-handed pattern on the ground plane . . . . .	29
4.4	S-parameter of a microstrip line with 2 row of triangle-shape left-handed pattern on the ground plane and interdigital capacitors on the stripline (red line represents $S_{21}$ and blue line represents $S_{11}$ . . . . .	30
4.5	S-parameter of a microstrip line with 2 row of flower-shape left-handed pattern etched on the ground plane and interdigital capacitors on the stripline (red line represents $S_{21}$ and blue line represents $S_{11}$ . . . . .	31
4.6	Top view of a microstrip line with 1 row of flower-shape left-handed pattern on the ground plane and interdigital capacitors on the stripline . . . . .	31
4.7	Bottom view of a microstrip line with 1 row of flower-shape left-handed pattern on the ground plane and interdigital capacitors on the stripline . . . . .	31
4.8	S-parameter of a microstrip line with 1 row of flower-shape left-handed pattern etched on the ground plane and interdigital capacitors on the stripline (red line represents $S_{21}$ and blue line represents $S_{11}$ . . . . .	32
4.9	Top view of the simulated antenna (blue part is substrate while pink part shows metal surface) . . . . .	32
4.10	Bottom view of the simulated antenna (blue part is substrate while pink part shows metal surface) . . . . .	33
4.11	Simulated $S_{11}$ against frequency of patch antenna with triangle shaped gaps on patch and strip bridges on ground . . . . .	33
4.12	Simulated VSWR against frequency of patch antenna with triangle shaped gaps on patch and strip bridges on ground . . . . .	34
4.13	Simulated antenna balance vs frequency in the working band . . . . .	34

4.14	Simulated 3D radiation pattern at the frequency of 7GHz . . . . .	35
4.15	Simulated 3D radiation pattern at the frequency of 8.1GHz . . . . .	35
4.16	Simulated radiation pattern at 7GHz on the plane of $\theta = 90^\circ$ . . . . .	36
4.17	Simulated radiation pattern at 8.1GHz on the plane of $\theta = 90^\circ$ . . . . .	36
4.18	Simulated radiation pattern at 7GHz on the plane of $\phi = 90^\circ$ . . . . .	37
4.19	Simulated radiation pattern at 8.1GHz on the plane of $\phi = 90^\circ$ . . . . .	38
4.20	Top view of the fabricated antenna ( $\varepsilon=2.2$ , substrate thickness $h=0.794\text{mm}$ , substrate size= $28.1\text{mm}\times 32\text{mm}$ , patch size= $12\text{mm}\times 16\text{mm}$ ) . . . . .	38
4.21	Bottom view of the fabricated antenna (width of gaps= $0.4\text{mm}$ ) . . . . .	39
5.1	Special device for measurements of angles of refractions . . . . .	40
5.2	3D view of SRR prism . . . . .	41
5.3	Top view of SRR prism . . . . .	41
A.1	Triangle pair and geometrical parameters associated with interior edge . . . . .	43
A.2	Geometry for construction of component of basis function normal to edge . . . . .	44
A.3	Local coordinates and edges for source triangle $T^q$ with the observation point in triangle $T^p$ . . . . .	46
A.4	Pair of tetrahedrons and geometrical parameters associated with $n$ th face . . . . .	49



# Chapter 1

## Introduction

Recently, left-handed material(LHM), which is also known as negative index media (NIM), has attracted a great deal of attention. These materials exhibit a negative refraction index  $n$ , and therefore can have very interesting properties, e.g., the phase and group velocities of electromagnetic waves in this material are opposite. Since the  $\mathbf{E}$  and  $\mathbf{H}$  fields and the wave vector  $\mathbf{k}$  of a propagating plane EM wave form a left-handed system in these materials, Veselago [1] introduced the term “left-handed materials” in his seminal work published in 1968. The interest in Veselago’s work was renewed since Pendry et al. [2] proposed an artificial material consisting of the so called split-ring resonators (SRRs) as shown in Figure 1.2, which exhibit a band of negative  $\mu$  values in spite of being made of non-magnetic materials and wires which provide the negative  $\varepsilon$  behavior. Based on Pendry’s suggestions and targeting the original idea of Veselago, Smith et al. demonstrated in 2000 the realization of the first left-handed material which consisted of an array of split ring resonators (SRRs) and thin wires in alternating layers [3]. To date, the range of imaginable applications of left-handed materials extends to the field of antenna design, vehicle coatings for altering radar cross section properties, and lenses [4].

Since the original microwave experiment of Smith et al., several LHMs were fabricated [5][6] that exhibited a pass band in which it was assumed that  $\varepsilon$  and  $\mu$  are both negative. This assumption was based on transmission measurements of the wires alone, the SRR alone, and the LHMs. The occurrence of a LHM transmission peak within the stop bands of the SRR and wire structures was taken as evidence for the appearance of LHM behavior. Further support to this interpretation was provided by the demonstration that such LHMs exhibit negative refraction of EM waves [7][8]. Moreover, there is a significant amount of numerical work [9][10][11][12] in which the transmission and reflection data are calculated for a finite length of metamaterial. A retrieval procedure can then be applied to obtain the metamaterial parameters  $\varepsilon$  and  $\mu$  under the assumption that it can be treated as homogeneous. This procedure was applied in [13] and confirmed that a medium composed of SRRs and wires could indeed be characterized by effective  $\varepsilon$  and  $\mu$  whose real parts were both negative over a finite frequency band, as was the real part of the refractive index  $n$ . However, it was recently shown [14] that the SRRs exhibit a resonant electric response in addition to their resonant magnetic response, and therefore, make the understanding and the fabrication of true LHMs more challenging.

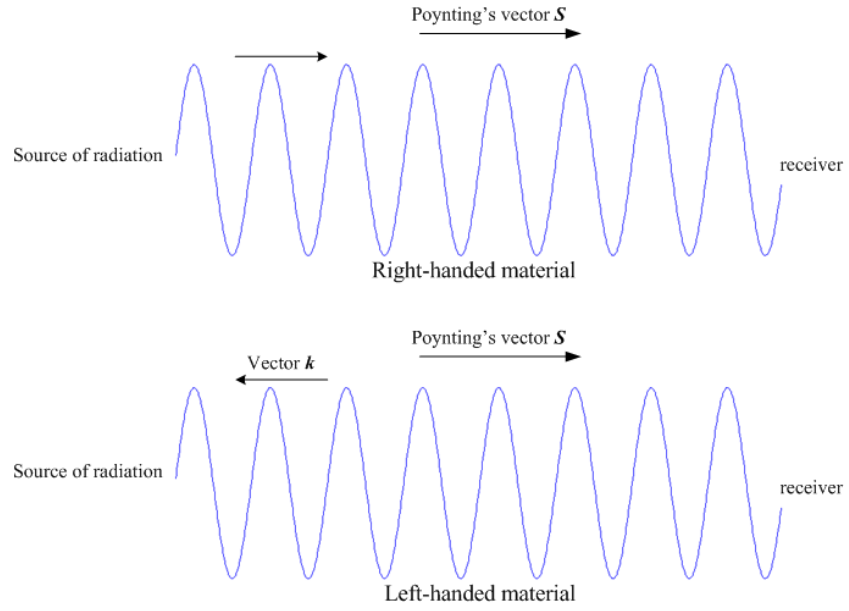


Figure 1.1: Poynting's vector and the wave vector for wave propagations in right-handed and left-handed materials.

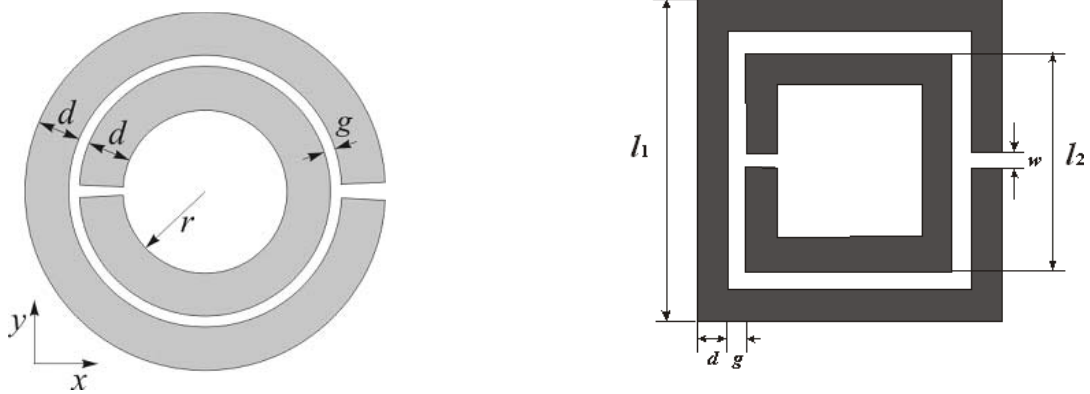


Figure 1.2: Round and square split-ring resonators

To design such artificial materials for different specific engineering applications, simulation tools are essential for saving efforts and costs. The numerical methods for characterizing these structures are still those fundamental numerical simulation techniques, i.e., the differential-equation (DE) method [15][16], the integral-equation (IE) method [17][18], and the equivalent-circuit models [19][20]. Among the three methods usually utilized for designing artificial synthetic materials, the electromagnetic solver developed based on the method of moments (MoM) for solving the hybrid volume-surface integral equation (VSIE)[21] is rigorous and widely adopted in various electromagnetic simulations. It is certainly a very good option for analyzing electromagnetic characteristics of metamaterials. The method of moment is one of the most popular numerical method for solving boundary-value problems in electromagnetic.

However, the MoM will lead to a full matrix whose numerical iterative solution requires  $O(N_{iter}N^2)$  operations and  $O(N^2)$  memory to store the matrix elements, where  $N$  and  $N_{iter}$  denote the number of unknowns and number of iterations, respectively [22]. The computational cost and memory requirement will increase much faster with the larger number of unknowns. On one hand, the operating frequency of electromagnetic waves in a medium of metamaterials falls usually within the microwave frequency band or even higher. On the other hand, the spacings and dimensions of conducting inclusions that compose the artificial media are required to be much smaller than the wave-length in order to synthesize a practical continuous material so that the number of inclusions is numerous and the resultant total number of unknowns is very large, even though the dimensions of such synthesized metamaterials are electrically small in this frequency band. To achieve this objective, a fast algorithm has to be integrated into the MoM procedure to accelerate the matrix-vector multiplications.

In Chapter 2, we discussed some special characteristic of split-ring resonators as well as the adaptive integral method (AIM). Here we AIM into the scattering problem of LHM. It was a fast integral-equation solver applicable to large-scale electromagnetic scattering problems which was described by Bleszynski [23][24] for the first time in 1996. In this approach, the field generated by a given current distribution is decomposed into near and far field components. The near field is computed using the conventional method of moments technique with the Galerkin discretization. The far field is calculated by approximating the original current distribution by an equivalent current distribution on a regular Cartesian grid, such that the two currents have identical multipole moments up to a required order  $m$ . As the result of this discretization, the original full impedance matrix is decomposed into a sum of a sparse matrix (corresponding to the near field component) and a product of sparse and Toeplitz matrices [25] (corresponding to the far field component). Because of the convolution nature of the Toeplitz kernel, the field generated by the equivalent current distribution can be then obtained by means of discrete Fast Fourier transforms.

In Chapter 3, we show the numerical result of our simulations based on this AIM algorithm. First, we design the size and shape of our structure. Then with AIM, we calculated the radar cross section (RCS) of a few SRR inclusions at an estimated frequency range to find the resonance frequency of this particular structure. At the vicinity of this frequency, we examine the RCS of a SRR slab with different kinds of plane-wave input. From the result, we find that when the input plane wave satisfy the magnetic resonance condition for SRR [14], the power can be transferred which satisfy the property of double-negative. However, when the input doesn't satisfy the resonance condition, the scattered electric field is very weak since the whole slab becomes no more than a ordinary scatterer. Then on one hand, this phenomenon obtained re-proved the LH

property of this SRR slab, on the other hand, it confirms that our AIM algorithm is an efficient and accurate solver to analyze composite LHM.

In Chapter 4, we present some newly designed left-handed structures and make necessary improvement to broaden the bandwidth. The new structure is applied in the fabrication of patch antenna to enhance the performance. Good agreements are achieved between simulation results and practical measurements. The antenna performs well with high gain, low loss and wide band.

In Chapter 5, future research topics and possible method is proposed.

## Chapter 2

# Split-Ring Resonators and Adaptive Integral Method

### 2.1 Split-Ring Resonators

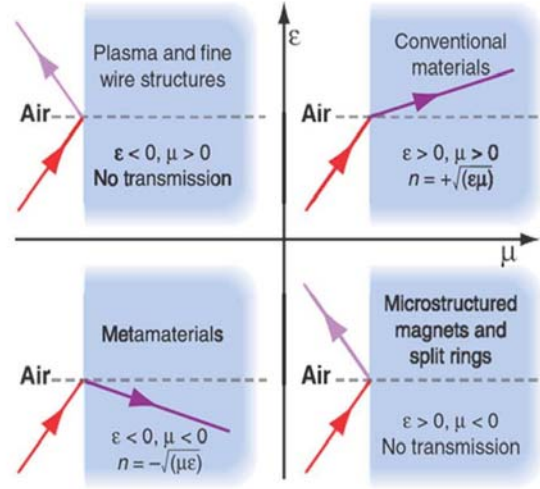
Currently, the metamaterials under study are composed of a periodic arrangement of metallic printed lines (or rods) that exhibit a negative permittivity, and split-ring resonators (SRRs) that exhibit a negative permeability. To understand how these metamaterials function, it is best to follow the historical steps that lead to the current geometry. First, it was shown that a 3-D array of thin, continuous (very long) metal wires exhibit a resonant frequency response similar to that of a plasma medium [26] [27]. At frequencies below the resonant frequency, the permittivity becomes negative, the wave vector is imaginary, and there is no transmission. Above the resonant frequency, the permittivity is real and transmission occurs. Second, it was demonstrated that negative permeability could be achieved using an array of SRRs [2]. The SRRs act like magnetic dipoles, with a resonant response resulting from internal inductance and capacitance. Close to resonance, the SRRs produce strong magnetic fields whose directions oppose the incident magnetic field, resulting in a negative effective permeability. Finally, once the negative permeability structures had been discovered, finding ways of combining them with negative permittivity structures was the next step in research, leading to the well known geometry shown in [28]. However, the demonstration of the LH properties of a metamaterial is not as straightforward as it seems, and showing that permittivity and permeability are separately negative over a similar frequency band does not imply that they remain so when the rods and SRRs are combined into a unique geometry. One of the first observations of the LH nature of these metamaterial structures was inferred by observing transmission and reflection coefficients over a wide frequency band. For the separate geometries (rods only or SRRs only), as shown in Figure 2.3 no transmission occurs because of an imaginary wave number. In the frequency band where the two parameters are simultaneously negative, transmission occurs when the combined geometry is considered. This band-pass phenomenon was indeed observed in these metamaterials [28]. However, as mentioned before, this transmission is not sufficient to conclude that the material is exhibiting LH behavior, since the interaction between the SRRs and rods could result in a positive permittivity and permeability, which would also yield transmission. To solve this problem Moss et al. did a more rigorous test to demonstrate the LH



Figure 2.1: Split-rings resonators with rods



Figure 2.2: Split-ring resonators with wires

Figure 2.3: Different combination of  $\varepsilon$  and  $\mu$ 

nature of a material [29] which show that the combination of SRRs and rods does yield a pass band of double negative. So, base on all these research result, we use SRR structure in further modeling and simulation.

## 2.2 Method of Moments

To design and compute the EM field of such artificial materials, simulation tools are essential for saving efforts and costs. The numerical methods for characterizing these structures are still those fundamental numerical simulation techniques, i.e., the differential-equation (DE) method [15][16], the integral-equation (IE) method [17][18], and the equivalent-circuit models [19][20]. Among the three methods usually utilized for designing artificial synthetic materials, the electromagnetic solver developed based on the method of moments (MoM) for solving the hybrid volume-surface integral equation (VSIE)[21] is rigorous and widely adopted in various electromagnetic simulations.

The method of moments (MoM) is a general procedure for solving linear equations. Consider the inhomogeneous equation

$$L(f) = g \quad (2.1)$$

where  $L$  is a linear operator,  $g$  is known, and  $f$  is to be determined. Let  $f$  be expanded in a series of functions  $f_1, f_2, f_3, \dots$  in the domain of  $L$ , as

$$f = \sum_n \alpha_n f_n \quad (2.2)$$

where the  $\alpha_n$  are constants. We shall call the  $f_n$  expansion functions or basis functions. For exact solution, (2.2) is usually an infinite summation and the  $f_n$  form a complete set of basis functions.

For approximate solution, (2.2) is a finite summation. Substituting (2.2) in (2.1), and using the linearity of  $L$ , we have

$$\sum_n \alpha_n L(f_n) = g \quad (2.3)$$

It is assumed that a suitable inner product  $\langle f, g \rangle$  has been determined for the problem. Now define a set of weighting functions, or testing functions,  $w_1, w_2, w_3, \dots$  in the range of  $L$  and take the inner product of (2.3) with each  $w_m$ . The result is

$$\sum_n \alpha_n \langle w_m, Lf_n \rangle = \langle w_m, g \rangle \quad (2.4)$$

$m = 1, 2, 3, \dots$  This set of equations can be written in matrix form as

$$[l_{mn}][\alpha_n] = [g_m] \quad (2.5)$$

where

$$[l_{mn}] = \begin{bmatrix} \langle w_1, Lf_1 \rangle & \langle w_1, Lf_2 \rangle & \cdots \\ \langle w_2, Lf_1 \rangle & \langle w_2, Lf_2 \rangle & \cdots \\ \cdots & \cdots & \cdots \end{bmatrix} \quad (2.6)$$

$$[\alpha_n] = \begin{bmatrix} \alpha_1 \\ \alpha_2 \\ \vdots \end{bmatrix} \quad [g_m] = \begin{bmatrix} \langle w_1, g \rangle \\ \langle w_2, g \rangle \\ \vdots \end{bmatrix} \quad (2.7)$$

If the matrix  $[l]$  is nonsingular its inverse  $[l^{-1}]$  exists. The  $\alpha_n$  are then given by

$$[\alpha_n] = [l_{nm}^{-1}][g_m] \quad (2.8)$$

and the solution for  $f$  is given by (2.2). For concise expression of this result, define the matrix of functions

$$[\tilde{f}_n] = [f_1 \quad f_2 \quad f_3 \quad \cdots] \quad (2.9)$$

and write

$$f = [\tilde{f}_n][l_{mn}^{-1}][g_m] \quad (2.10)$$

This solution may be exact or approximate, depending upon the choice of the  $f_n$  and  $w_n$ . The particular choice  $w_n = f_n$  is known as the Galerkin's method.

If the matrix  $[l]$  is of infinite order, it can be inverted only in special cases, for example, if it is diagonal. The classical eigenfunction method leads to a diagonal matrix, and can be thought of as a special case of the method of moments. If the sets  $f_n$  and  $w_n$  are finite, the matrix is of finite order, and can be inverted by known method.

One of the main tasks in many particular problem is the choice of the  $f_n$  and  $w_n$ . The  $f_n$  should be linearly independent and chosen so that some superposition can be approximated  $f$  reasonably



well. The  $w_n$  should also be linearly chosen so that the products  $\langle w_n, g \rangle$  depend on relatively independent properties of  $g$ . Some additional factors which affect the choice of  $f_n$  and  $w_n$  are the accuracy of solution desired, the ease of evaluation of the matrix elements, the size of the matrix that can be inverted, and the realization of a well-conditioned matrix [l]

However, the MoM will lead to a full matrix. The matrix equation can be solved using a conventional direct solver or an iterative solver. A direct solver requires  $O(N^3)$  operations to solve the equation while an iterative solver requires  $O(N_{iter}N^2)$  operations. Both solvers require  $O(N^2)$  memory storage to store the matrix elements where  $N$  and  $N_{iter}$  denote the number of unknowns and number of iterations, respectively [22]. These stringent requirements have prevented the use of the conventional MoM to solve problems with a large number of unknowns. The computational cost and memory requirement will increase much faster with the larger number of unknowns. On one hand, the operating frequency of electromagnetic waves in a medium of metamaterials falls usually within the microwave frequency band or even higher. On the other hand, the spacings and dimensions of conducting inclusions that compose the artificial media are required to be smaller than the wave-length in order to synthesize a practical continuous material so that the number of inclusions is numerous and the resultant total number of unknowns is very large, even though the dimensions of such synthesized metamaterials are electrically small in this frequency band. To achieve this objective, a fast algorithm has to be integrated into the MoM procedure to accelerate the matrix-vector multiplications.

## 2.3 Adaptive Integral Method

### 2.3.1 the Advantages of Adaptive Integral Method (AIM)

There are three major fast algorithms recently developed to overcome the problem of large memory requirement and computational complexity caused by MoM.

1) Fast multipole method (FMM) [30, 31] and its extension, multilevel fast multipole algorithm (MLFMA) [32], exhibit computational complexity on the order of  $O(N^{1.5})$  and  $O(N \log N)$ , respectively. However, a large value of  $N$  is required to gain advantage over the MoM, and certainly this is satisfied mostly when the FMM or MLFMA is employed.

2) Conjugate gradient fast Fourier transform (CG-FFT) as a grid-based fast algorithm has been also used widely to solve the scattering problem formulated by surface integral equation (SIE) and volume integral equation (VIE) [33]. The attracting feature of CG-FFT is the memory requirement and computational complexity are of  $O(N \log N)$  and  $O(N)$ , respectively. However, the major drawback of this method is the staircase approximation due to the usage of uniform rectangular grid to model arbitrarily shaped object, and therefore the resulted staircase error.

3) The adaptive integral method (AIM) has been proposed to overcome the shortcomings of CG-FFT. It was initially proposed to solve scattering problem of conducting objects [23, 24]. The AIM and its counterpart, precorrected FFT (P-FFT), were also used to solve the other problem formulated using the surface integral equation (SIE) [34]. Recently, Zhang and Liu have used the AIM to solve the scattering problem formulated using VIE [35]. The computational complexity for AIM is  $O(N^{1.5} \log N)$  and  $O(N \log N)$  for surface and volume scatterers, respectively.

Later in this report, this AIM will be applied for computing the electromagnetic scattering by the SRR structures to examine their LH property.

### 2.3.2 Introduction of Hybrid Volume-Surface Integral Equation

The scattering problem of mixed dielectric and conducting objects can be formulated using SIE or the combination VIE and SIE. The scattering by conducting objects is usually characterized by using the SIE, but the choice of using SIE or VIE for dielectric object depends on its inhomogeneity. For an object with arbitrary inhomogeneity, solving the scattering problem using VIE will be more advantageous than SIE, as the latter requires the integral equations to be formulated in every dielectric regions. However, if the object consists of only piecewise homogeneous dielectric materials, then SIE formulation is generally preferred. The formulation of mixed dielectric and conducting object problem using only SIE can be found in the literature [36][37]. Another formulation that involves both the VIE and SIE was made to describe the scattering by dielectric and conducting bodies and then to combine them together to form hybrid volume-surface integral equation (VSIE) [38]. We found this method is useful to SRR structure since VIE and SIE can be applied to describe the EM field in the dielectric region and conducting surface separately.

And, for closed conducting body, the combined field integral equation (CFIE) can be used as it eliminates interior resonance problem and it normally yields a better conditioned matrix equation as compared to electric field integral equation (EFIE) or magnetic field integral equation (MFIE). However, for the open conducting body like SRR, the MFIE can not be used. So here we use EFIE only for SIE.

### 2.3.3 Formulations For Hybrid Volume-Surface Integral Equation

In this section, we discuss the formulations for VSIE.

First, we consider a general case of an arbitrarily shaped three-dimensional (3-D) scatterer, which consists of homogeneous or inhomogeneous dielectric material and conducting body as shown in Figure 2.4. The object is embedded in an isotropic homogeneous background medium with permittivity  $\varepsilon_b$  and permeability  $\mu_b$ . The scatterer is illuminated by an incident wave  $\mathbf{E}^{inc}$ , which is excited by impressed sources in the background media. The dielectric region  $V$  is assumed to have the permeability  $\mu = \mu_b$  and complex dielectric constant  $\tilde{\varepsilon} = \varepsilon(r) - j\sigma(r)/\omega$  where  $\varepsilon(r)$  and  $\sigma(r)$  are permittivity and conductivity, respectively, at  $\mathbf{r}$ . Inside the dielectric region  $V$  and on the surface of conducting body  $S$ , the incident wave induces volume current  $\mathbf{J}_V$  and surface current  $\mathbf{J}_S$ . The scattered electric field  $\mathbf{E}^{sca}$  and magnetic field  $\mathbf{H}^{sca}$  produced by the induced volume and surface currents are given by

$$\mathbf{E}_{\Omega}^{sca}(\mathbf{r}) = -jk_b\eta_b\mathbf{A}_{\Omega}(\mathbf{r}) - \nabla\Phi_{\Omega}(\mathbf{r}), \quad \Omega = S \text{ or } V \quad (2.11)$$

$$\mathbf{H}_{\Omega}^{sca}(\mathbf{r}) = \nabla \times \mathbf{A}_{\Omega}(\mathbf{r}), \quad \Omega = S \text{ or } V \quad (2.12)$$

where the magnetic vector potential is defined as:

$$\mathbf{A}_{\Omega}(\mathbf{r}) = \int_{\Omega} \mathbf{J}_{\Omega}(\mathbf{r}')g(\mathbf{r}, \mathbf{r}')d\mathbf{r}', \quad \Omega = S \text{ or } V \quad (2.13)$$

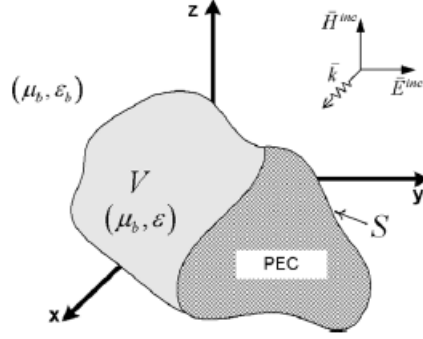


Figure 2.4: Geometry of scatterer consisting of dielectric material and conducting body embedded in an isotropic homogeneous medium

and the electric scalar potential is defined as:

$$\Phi_{\Omega}(\mathbf{r}) = -\frac{\eta_b}{jk_b} \int_{\Omega} \nabla' \cdot \mathbf{J}_{\Omega}(\mathbf{r}') g(\mathbf{r}, \mathbf{r}') d\mathbf{r}', \quad \Omega = S \text{ or } V \quad (2.14)$$

with  $g(\mathbf{r}, \mathbf{r}') = \frac{e^{-jk_b|\mathbf{r}-\mathbf{r}'|}}{4\pi|\mathbf{r}-\mathbf{r}'|}$ ,  $\eta_b = \sqrt{\frac{\mu_b}{\varepsilon_b}}$ , and  $k_b$  as the wavenumber of background medium

In the dielectric region  $V$ , by taking the scattered field from the surface current into consideration, the total electric field becomes

$$\mathbf{E}(\mathbf{r}) = \mathbf{E}^{inc}(\mathbf{r}) + \mathbf{E}_V^{sca}(\mathbf{r}) + \mathbf{E}_S^{sca}(\mathbf{r}) \quad (2.15)$$

and the induced volume current is defined as

$$\mathbf{J}_V = j\omega(\tilde{\varepsilon} - \varepsilon_b)\mathbf{E} \quad (2.16)$$

Similarly, the scattered field by induced volume current also contributes to the total field on  $S$ . Since the tangential components of total electric field vanish on conducting surface, we get

$$\hat{\mathbf{n}} \times \mathbf{E}^{inc}(\mathbf{r}) = -\hat{\mathbf{n}} \times \mathbf{E}_V^{sca}(\mathbf{r}) - \hat{\mathbf{n}} \times \mathbf{E}_S^{sca}(\mathbf{r}) \quad (2.17)$$

Equations 2.15 and 2.17 are known as the EFIE as the formulations involve only electric field. For a closed conducting surface, the MFIE can be obtained by considering the tangential components of the total magnetic field on the conducting surface, which are equal to the induced surface current components. Since we'll not use MFIE here, we do not list the equations here.

### 2.3.4 RWG and SWG basis function

As we mentioned in the section of MoM, we must have basis functions to expand the current on conducting surface and dielectric volume. These basis functions must be associated with the surface and volume element we get after discretization. Here in our problem, the volume of dielectric material and surface of conducting body are discretized into tetrahedral elements and triangular

patches, respectively. These elements are used because of their flexibility to model arbitrarily shaped 3-D object. Then the surface current is expanded using vector basis function  $f_S$ , which has constant-normal and linear-tangential (CN/LT) components along the edge

$$\mathbf{J}_S = \sum_{n=1}^{N_S} I_n^S \mathbf{f}_n^S \quad (2.18)$$

As for the dielectric region, the electric flux  $\mathbf{D}$  is expanded using appropriate volume CN/LT basis functions  $f_V$  as follows:

$$\mathbf{D} = \tilde{\varepsilon}(\mathbf{r})\mathbf{E} = \sum_{n=1}^{N_V} I_n^V \mathbf{f}_n^V \quad (2.19)$$

by use of equation 2.16, the induced volume current is expressed as

$$\mathbf{J}_V = j\omega \sum_{n=1}^{N_V} \frac{\tilde{\varepsilon}(\mathbf{r}) - \varepsilon_0}{\tilde{\varepsilon}(\mathbf{r})} I_n^V \mathbf{f}_n^V = j\omega \sum_{n=1}^{N_V} \kappa(\mathbf{r}) I_n^V \mathbf{f}_n^V \quad (2.20)$$

where  $\kappa(\mathbf{r}) = \frac{\tilde{\varepsilon}(\mathbf{r}) - \varepsilon_0}{\tilde{\varepsilon}(\mathbf{r})}$  is the contrast ratio and  $\tilde{\varepsilon}(\mathbf{r})$  is the permeability of a tetrahedron element.

In this report, the CN/LT basis functions that have been used are SWG basis function [39] and RWG basis function [40] for the induced volume current and surface current, respectively. The SWG basis function is defined on a pair of tetrahedral elements while the RWG basis function is defined on a pair of triangular patches. The properties of SWG and RWG basis functions for example, the continuity of the electric flux density normal to the interior face (SWG) and the continuity of the surface current normal to the interior edge (RWG) make them suitable to efficiently discretize the previous integral equations. The formulas for SWG and RWG basis function as well as the testing procedure we used in our simulation program will not be list here since these complicated formulas are not our main point. However, they can be found in the Appendix. It is also noted that during discretization of the object, the triangular patches are generated such that it is coincided with the surface of tetrahedron. Using the volume basis function to test (2.15) and the surface basis function to test (2.17), the hybrid integral equations will be converted into a matrix equation system as:

$$\begin{bmatrix} \bar{\mathbf{Z}}^{VV} & \bar{\mathbf{Z}}^{VS} \\ \bar{\mathbf{Z}}^{SV} & \bar{\mathbf{Z}}^{SS} \end{bmatrix} \begin{bmatrix} \mathbf{I}^V \\ \mathbf{I}^S \end{bmatrix} = \begin{bmatrix} \mathbf{E}^V \\ \mathbf{E}^S \end{bmatrix} \quad (2.21)$$

where the vectors  $\mathbf{I}^V$  and  $\mathbf{I}^S$  represent the coefficients of volume current and surface current respectively. The excitation vector can be computed using

$$E_m^V = \int_{V_m} \mathbf{f}_m^V \cdot \mathbf{E}^{inc}(\mathbf{r}') d\mathbf{r}' \quad (2.22)$$

$$E_m^S = \int_{S_m} \mathbf{f}_m^S \cdot \mathbf{E}^{inc}(\mathbf{r}') d\mathbf{r}' \quad (2.23)$$

while the elements of the block matrices in (2.21) can be computed using the formulas shown below:

$$Z_{mn}^{VV} = \int_{V_m} \frac{\mathbf{f}_m^V \mathbf{f}_n^V}{\tilde{\epsilon}} dr - \omega k_b \eta_b \int_{V_m} \mathbf{f}_m^V \left[ \int_{V_n} \kappa \mathbf{f}_n^V g(\mathbf{r}, \mathbf{r}') dr' + \frac{\nabla}{k_b^2} \int_{V_n} \nabla' \cdot (\kappa \mathbf{f}_n^V) g(\mathbf{r}, \mathbf{r}') \right] dr \quad (2.24a)$$

$$Z_{mn}^{VS} = j k_b \eta_b \int_{V_m} \mathbf{f}_m^V \cdot \left[ \int_{S_n} \mathbf{f}_n^S g(\mathbf{r}, \mathbf{r}') dr' + \frac{\nabla}{k_b^2} \int_{S_n} \nabla' \cdot \mathbf{f}_n^S g(\mathbf{r}, \mathbf{r}') dr' \right] dr \quad (2.24b)$$

$$Z_{mn}^{SV} = -\omega k_b \eta_b \int_{S_m} \mathbf{f}_m^S \cdot \left[ \int_{V_n} \kappa \mathbf{f}_n^V g(\mathbf{r}, \mathbf{r}') dr' + \frac{\nabla}{k_b^2} \int_{V_n} \nabla' \cdot (\kappa \mathbf{f}_n^V) g(\mathbf{r}, \mathbf{r}') dr' \right] dr \quad (2.24c)$$

$$Z_{mn}^{SS} = j k_b \eta_b \int_{S_m} \mathbf{f}_m^S \cdot \left[ \int_{S_n} \mathbf{f}_n^S g(\mathbf{r}, \mathbf{r}') dr' + \frac{\nabla}{k_b^2} \int_{S_n} \nabla' \cdot \mathbf{f}_n^S g(\mathbf{r}, \mathbf{r}') dr' \right] dr \quad (2.24d)$$

$\kappa$  is a constant value within the tetrahedron and can be taken out from the integration.

Besides, we can also write

$$\nabla \cdot (\kappa \mathbf{f}_n^V) = \kappa \nabla \cdot \mathbf{f}_n^V + \nabla \kappa \cdot \mathbf{f}_n^V \quad (2.25)$$

and the second term given by 2.25 as:

$$\nabla \kappa \cdot \mathbf{f}_n^V = \begin{cases} I_n^V (\kappa_n^+ - \kappa_n^-), & \text{on the common facet} \\ 0, & \text{elsewhere} \end{cases} \quad (2.26)$$

### 2.3.5 Formulations for AIM

The AIM has been used to reduce the memory requirement and to accelerate the matrix-vector multiplication in iterative solver. The basic idea of AIM is to approximate the far-zone interaction using the FFT, and then to compute the near-zone interaction directly. This matrix-vector multiplication can be split into two parts, i.e.

$$\bar{\mathbf{Z}} \mathbf{I} = \bar{\mathbf{Z}}^{near} \mathbf{I} + \bar{\mathbf{Z}}^{far} \mathbf{I} \quad (2.27)$$

where  $\bar{\mathbf{Z}}^{near}$  is a sparse matrix that contains only the nearby elements within a threshold distance and  $\bar{\mathbf{Z}}^{far}$  represents the farzone interaction of the elements.

The matrix-vector multiplication implemented inside the AIM solver can be summarized using the following steps [41]:

- project the patch currents, either using multipole [23] expansion or far-field matching[42], to the surrounding grids;
- compute the grid potentials using FFT;
- interpolate the potentials back to the patch; and

- compute the correct near-field interaction for each of the patches.

To employ the AIM, the object is enclosed in a rectangular grid and then recursively subdivided into small rectangular grids. In order to use FFT to approximate the far-zone interaction, we need to transform the SWG and RWG basis functions into the Cartesian grids. It is noted that by using vector identity and divergence theorem, the  $\nabla$  operator in (2.24) can be shifted and operated on the testing function [39], [40]. Hence we can denote  $\gamma_n$  to represent any one of the components  $\{\mathbf{f}^S, \kappa \mathbf{f}^V, \nabla \cdot (\kappa \mathbf{f}_V)\}$  and express all the matrix elements in (2.24) in the following unified form:

$$Z_{mn} = \int_{\alpha_m} \int_{\alpha_n} \gamma_m(\mathbf{r}) g(\mathbf{r}, \mathbf{r}') \gamma_n(\mathbf{r}') d\mathbf{r}' d\mathbf{r} \quad (2.28)$$

The transformation function  $\gamma_n(\mathbf{r})$  can be approximated as a linear combination of Dirac delta functions, i.e.

$$\gamma_n(\mathbf{r}) \approx \hat{\gamma}(\mathbf{r}) = \sum_{u=1}^{(m+1)^3} \Lambda_{nu} \delta(\mathbf{r} - \mathbf{r}') \quad (2.29)$$

where  $M$  is the expansion order and  $\Lambda_{nu}$  denotes the expansion coefficients of  $\gamma_n(\mathbf{r})$ .  $\Lambda_{nu}$  can be determined using the multipole expansion or far-field approximation [34]. The multipole expansion method is based on the criterion that the coefficients  $\Lambda_{nu}$  produce the same multipole moments of the original basis function

$$\begin{aligned} & \int_{\alpha_n} \gamma_n(\mathbf{r}) (x - x_0)^{m_1} (y - y_0)^{m_2} (z - z_0)^{m_3} d\mathbf{r} \\ &= \sum_{u=1}^{(m+1)^3} (x_{nu} - x_0)^{m_1} (y_{nu} - y_0)^{m_2} (z_{nu} - z_0)^{m_3} \Lambda_{nu} \\ & \text{for } 0 \leq \{m_1, m_2, m_3\} \leq M \end{aligned} \quad (2.30)$$

where the reference point  $r_0 = (x_0, y_0, z_0)$  is chosen as the center of the basis function. The far-field approximation method matches the far-fields produced by  $\gamma_n(\mathbf{r})$  and  $\hat{\gamma}_n(\mathbf{r})$  on a unit sphere, and it thus obtains the expansion coefficients. Once the transformation function has been determined, the matrix elements can be approximated as

$$\hat{Z}_{mn} = \sum_{v=1}^{(m+1)^3} \sum_{u=1}^{(m+1)^3} \Lambda_{mv} g(\mathbf{r}_v, \mathbf{r}'_u) \Lambda_{nu} \quad (2.31)$$

By using the transformation function, now we are able to compute the two components in the matrix-vector multiplication in A.12 with

$$\bar{\mathbf{Z}}^{far} = \bar{\Lambda} \bar{\mathbf{g}} \bar{\Lambda}^T \quad (2.32a)$$

$$\bar{\mathbf{Z}}^{near} = \bar{\mathbf{Z}}_{nz}^{MoM} - \bar{\mathbf{Z}}^{far} \quad (2.32b)$$

where  $\bar{\mathbf{Z}}_{near}$  is the matrix containing only the direct interaction of neighbor elements and  $\bar{\Lambda}$  represents the basis transformation matrix of the elements. The matrix  $\bar{\mathbf{g}}$  is Toeplitz, and this

enables the use of FFT to compute the 3-D convolution in the 2.32a efficiently. Hence we can represent the matrix-vector multiplication as

$$\begin{aligned}\bar{\mathbf{Z}}\mathbf{I} &= \bar{\mathbf{Z}}^{near}\mathbf{I} + \bar{\mathbf{Z}}^{far}\mathbf{I} \\ &= \bar{\mathbf{Z}}^{near}\mathbf{I} + \bar{\mathbf{\Lambda}}\mathfrak{S}^{-1}\left\{\mathfrak{S}\{\bar{\mathbf{g}}\} \cdot \mathfrak{S}\{\bar{\mathbf{\Lambda}}^T\mathbf{I}\}\right\}\end{aligned}\tag{2.33}$$

where  $\mathfrak{S}\{\bullet\}$  and  $\mathfrak{S}^{-1}\{\bullet\}$  stand for FFT and inverse FFT respectively.

## Chapter 3

# Numerical Result for AIM

### 3.1 Validation of the VSIE-AIM Algorithm

An example is considered for validating the accuracy of the code developed. We consider a coated dielectric sphere having a radius of 1 m. The core of the sphere has a radius of 0.9 m and a relative permittivity of  $\epsilon_{r1} = 1.4 - 0.3j$ , and the thickness of coating layer is 0.1m with a relative permittivity of  $\epsilon_{r2} = 1.6 - 0.8j$ . The bistatic radar cross section(RCS) for the VV- and HH-polarizations at 750 MHz are computed and the results are shown in Figure 3.1. The results are compared with Mie series solutions and good agreements have been observed in the comparisons. So, in the next step we apply this algorithm in the scattering problem of SRR structure.

### 3.2 Resonance Frequency of SRRs

#### 3.2.1 Geometry Statement of SRR structure

Here we choose square shape SRR structure instead of round shape SRR structure since the it is easier to mesh and hence, easier for us to get an accurate result since when we mesh the conducting surface into triangular patches without any mesh-induced segment and apply the SWG basis function to the patches.

#### 3.2.2 Resonance Frequency of SRRs

First, we consider one row of SRR structure (3 inclusions placed side by side along y-). The geometry and dimensions of this kind of inclusions are shown in Figure 3.2. The width of all metal strips is 0.25mm, the thickness of dielectric is 0.254mm and the length of each dielectric square is 3.3mm. All the rings and wires are place at the center of each dielectric square. The relative permittivity of dielectric is set to be  $\epsilon = 1$ .

We examine the scattering cross section (SCS) [9] of this row of 3 elements and plot it verses frequency in Figure 3.5. It can be seen that the resonant frequency is approximately 15.80 GHz.



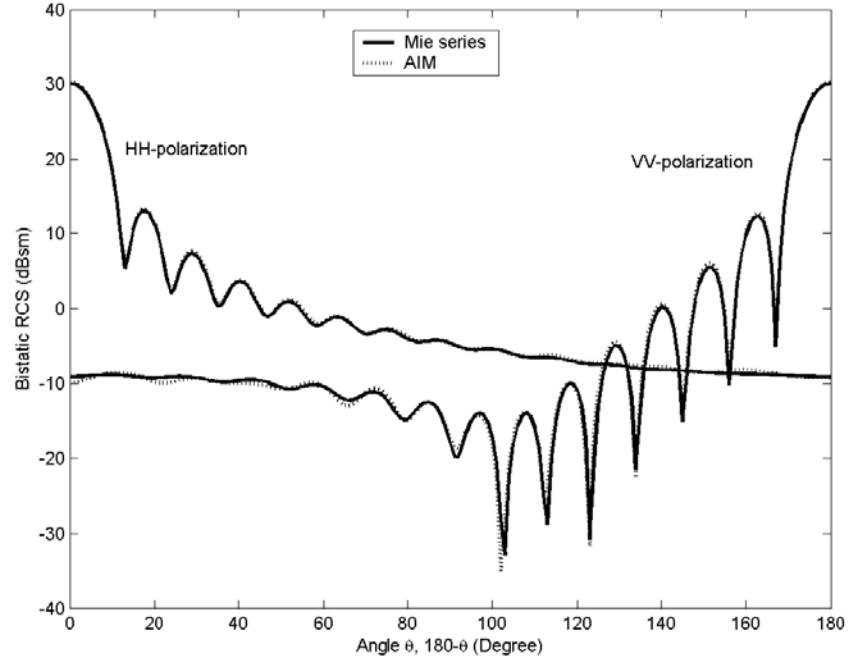


Figure 3.1: Bistatic RCS of a coated dielectric sphere ( $a_1 = 0.9$  m,  $\varepsilon_{r1} = 1.4 - 0.3j$ ;  $a_2 = 1$  m,  $\varepsilon_{r2} = 1.6 - 0.8j$ ) at 750 MHz.

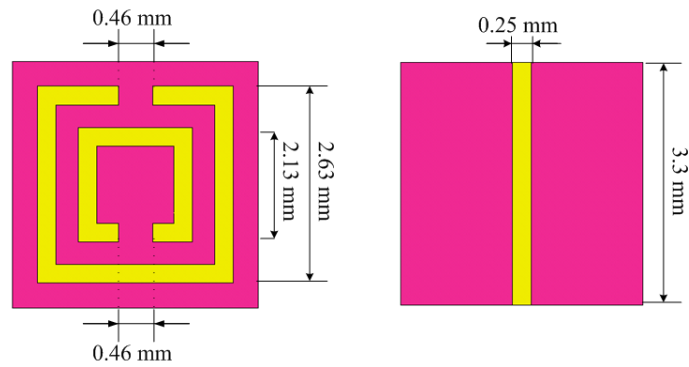


Figure 3.2: The front and back view of 1 SRR inclusion

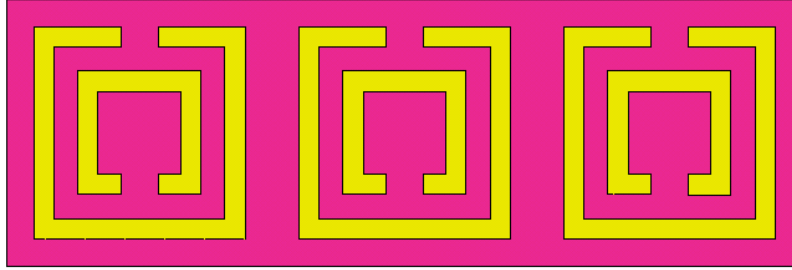


Figure 3.3: The rings view of 1 row of SRRs (inclusions)

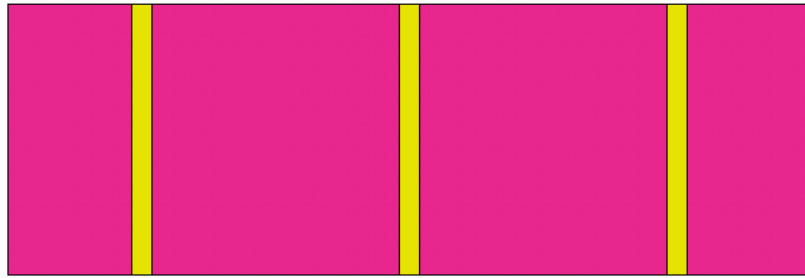
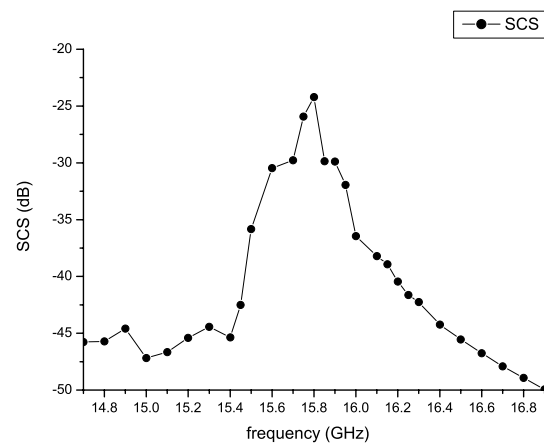


Figure 3.4: The wire view of 1 row of SRRs (inclusions)

Figure 3.5: SCS versus frequency for a row of inclusions (3 SRRs) at  $\theta = \phi = 90^\circ$

### 3.3 RCS of a SRR Slab With Different Plane-Waves as Illuminator

Next, at this resonant frequency, we analyze the propagation characteristics of electromagnetic wave in a LHM sample placed in the free space. It's a LHM slab composed of many rows of inclusions shown in Figure 3.2. The 3-D view of this slab is depicted in 3.6. The space distances of the inclusions denoted, respectively, by  $d_x$ ,  $d_y$  and  $d_z$  in the  $x$ -,  $y$ - and  $z$ - directions, are all 3.3 mm. There are totally 54 SRR elements which are arranged into 18 rows along  $x$ - and 3 columns along  $y$ -. In order to show that our AIM algorithm is suitable for this structure, we illuminate the slab with two different plane waves coming from  $-y$  direction as shown in Figure 3.6, and then we check the RCS of this SRR slab in each case. Actually, SRR requires the electric field  $\mathbf{E}^{inc}$  in parallel with the plane of the ring ( $yOz$  plane) to get maximum magnetic resonant. In other words, the rings are not supposed to be on the  $H-k$  plane [14]. So if  $\mathbf{E}^{inc}$  is perpendicular with the plane of rings as show in case < 2 >, the RCS must be very small and the whole structure becomes no more than an ordinary scatterer which does not acquire negative refractive index. Figure 3.3 to Figure 3.10 show values of  $E_z$  and RCS when the illuminators are of case < 1 > and case < 2 > respectively.

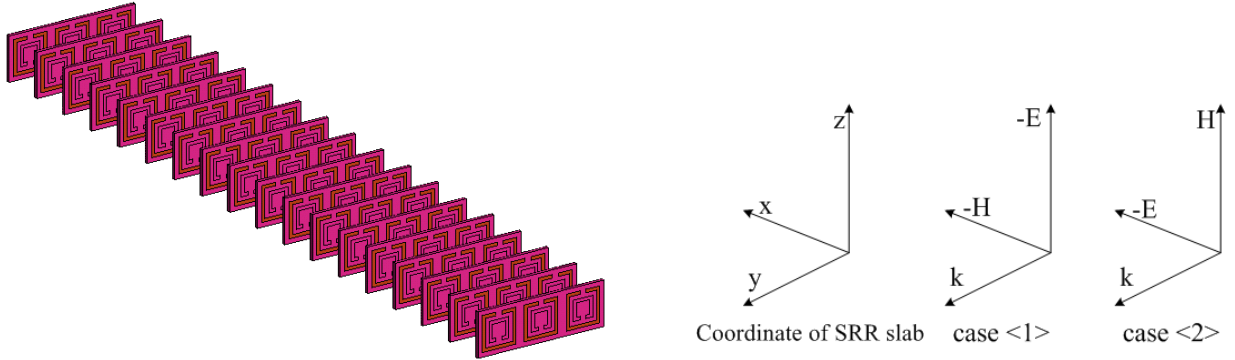


Figure 3.6: Structure of the slab composed by SRRs and wires with and two different incidents in the reference frame

Another advantage of our program compared with other algorithm is that we include volume element here. Thus, we can change the  $\varepsilon$  to observe the change of  $E_z$  and RCS very conveniently. Here we use  $\varepsilon = 1.60 - 0.05j$  instead of  $\varepsilon = 1$ . Below are the plot of  $E_z$  and RCS versus  $\phi$  at 15.8 GHz when the input are of case < 1 > and case < 2 > respectively.

Further more, Figures 3.15-3.18 listed below show the  $E_z$  and RCS of  $\varepsilon = 2.40 - 0.20j$  at 15.8 GHz when the slab under magnetic resonance and no magnetic resonance input respectively. Before calculating the scattering field of this material, we first examine the resonant frequency again to ensure the new slab works in the pass band of resonance. We found that the central frequency changes less than 0.1GHz which is actually a very small number compared with the central frequency. So, we can still fix the frequency at 15.8 GHz which is in the pass band. From the  $E_z$  and RCS result, we can observe a decrease in the scattering field which is due to higher permittivity.

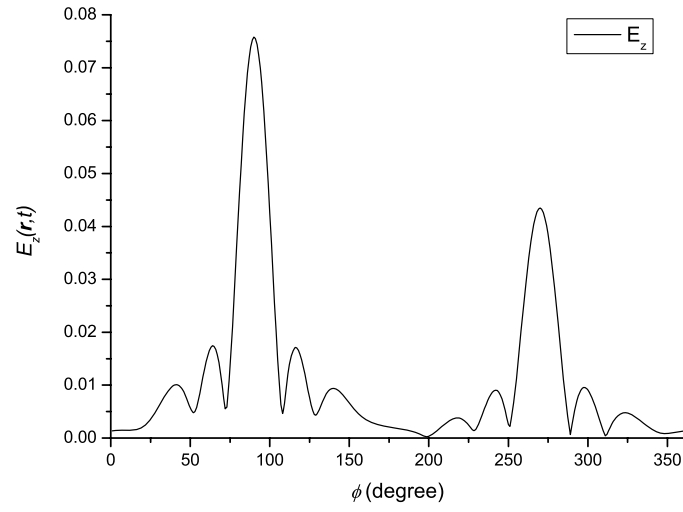
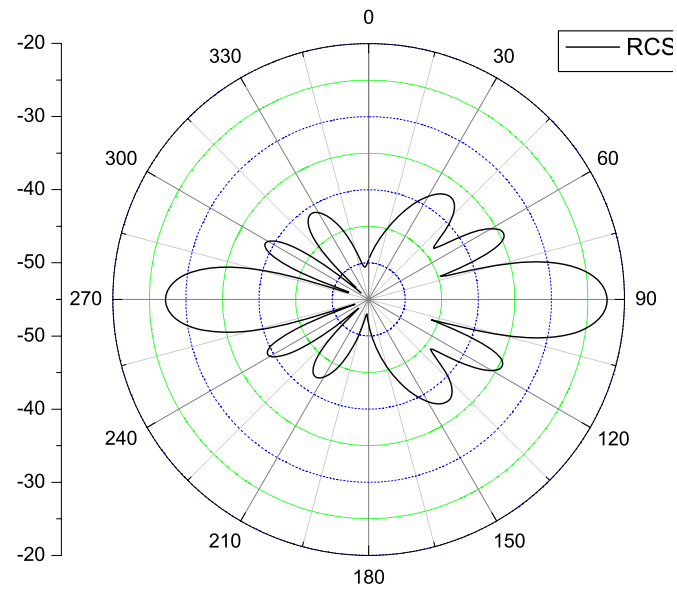
Figure 3.7:  $E_z$  of the slab of case < 1 > at 15.8 GHz

Figure 3.8: RCS of the slab of case &lt; 1 &gt; at 15.8 GHz

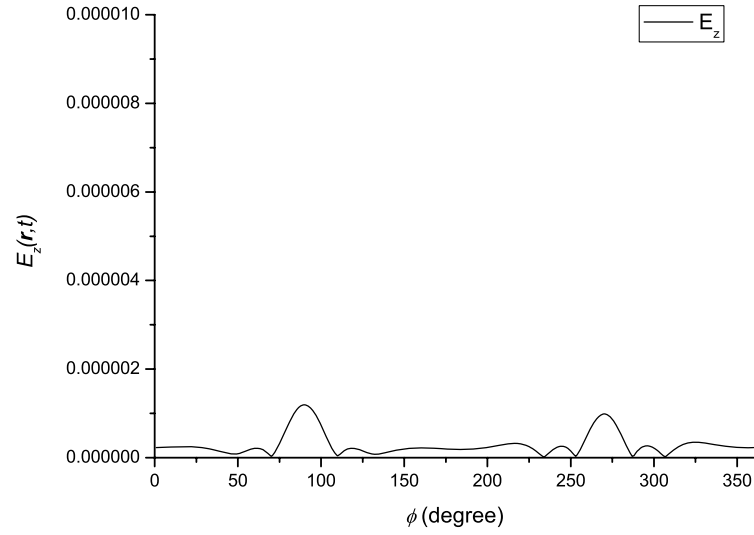
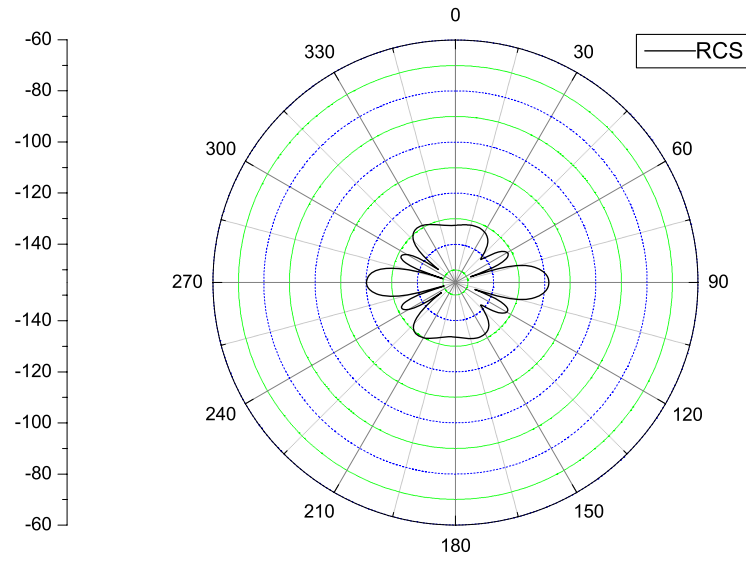
Figure 3.9:  $E_z$  of the slab of case < 2 > at 15.8 GHz

Figure 3.10: RCS of the slab of case &lt; 2 &gt; at 15.8 GHz

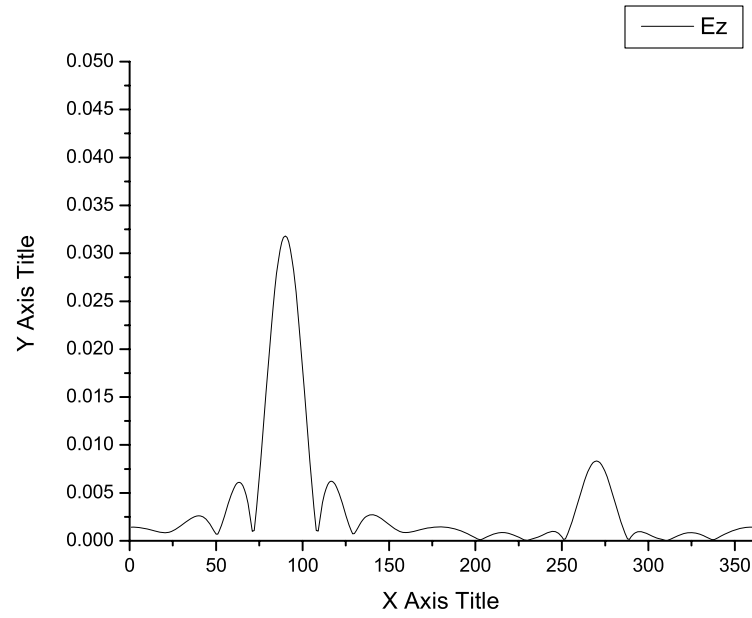


Figure 3.11:  $E_z$  of the slab of case < 1 > at 15.8 GHz when  $\varepsilon = 1.60 - 0.05j$

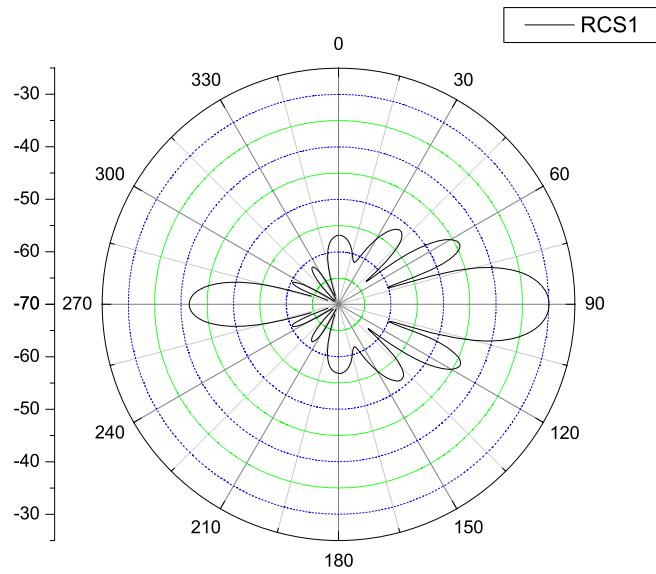


Figure 3.12: RCS of the slab of case < 1 > at 15.8 GHz when  $\varepsilon = 1.60 - 0.05j$

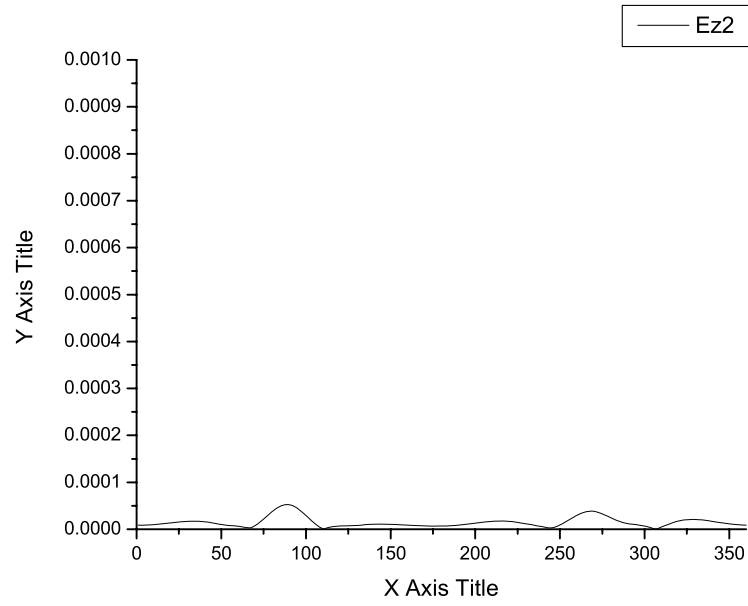


Figure 3.13:  $E_z$  of the slab of case < 2 > at 15.8 GHz when  $\varepsilon = 1.60 - 0.05j$

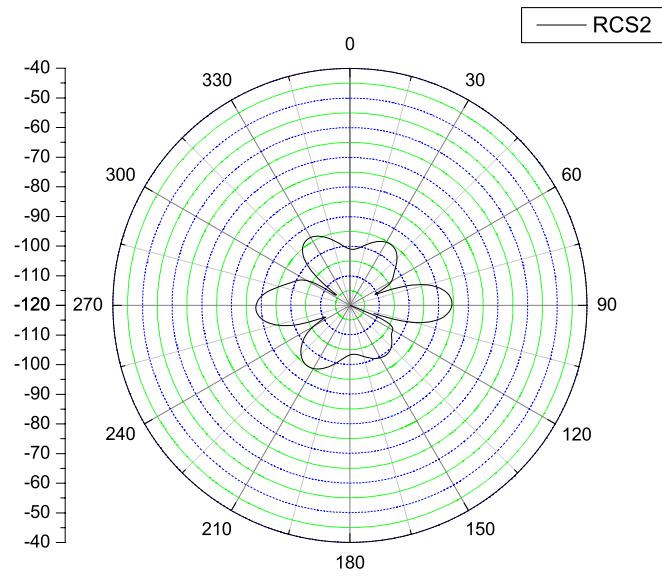


Figure 3.14: RCS of the slab of case < 2 > at 15.8 GHz when  $\varepsilon = 1.60 - 0.05j$

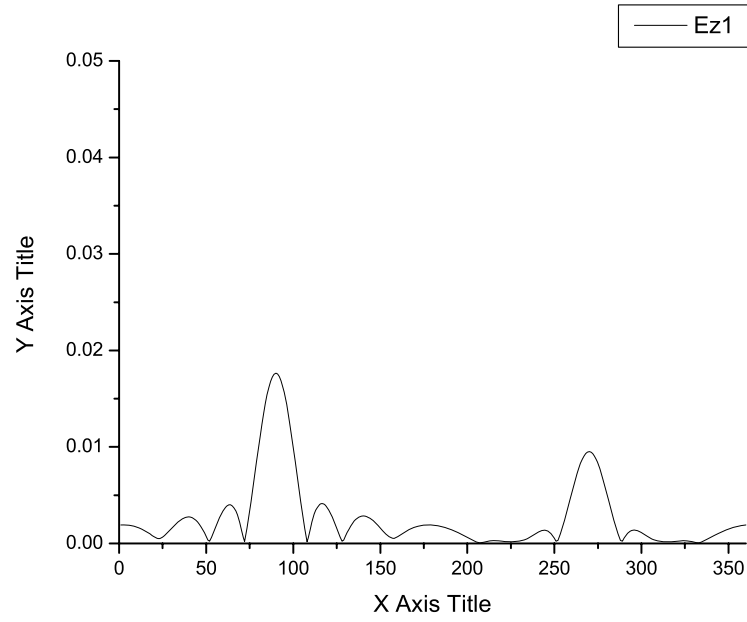


Figure 3.15:  $E_z$  of the slab of case < 1 > at 15.8 GHz when  $\varepsilon = 2.40 - 0.20j$

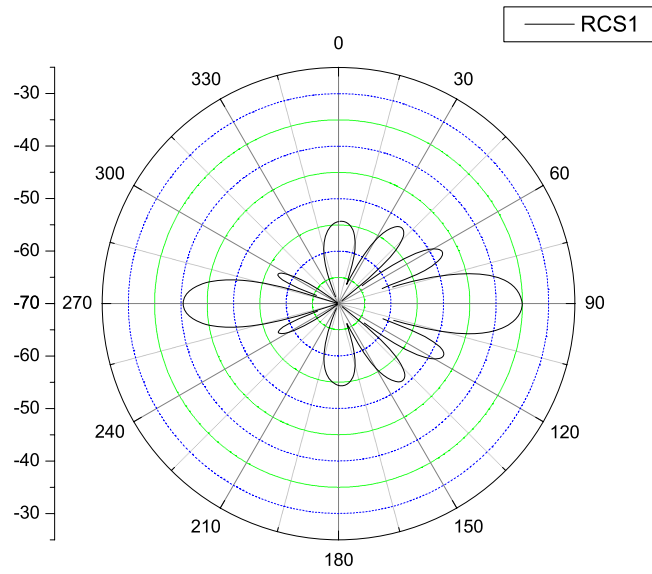


Figure 3.16: RCS of the slab of case < 1 > at 15.8 GHz when  $\varepsilon = 2.40 - 0.20j$



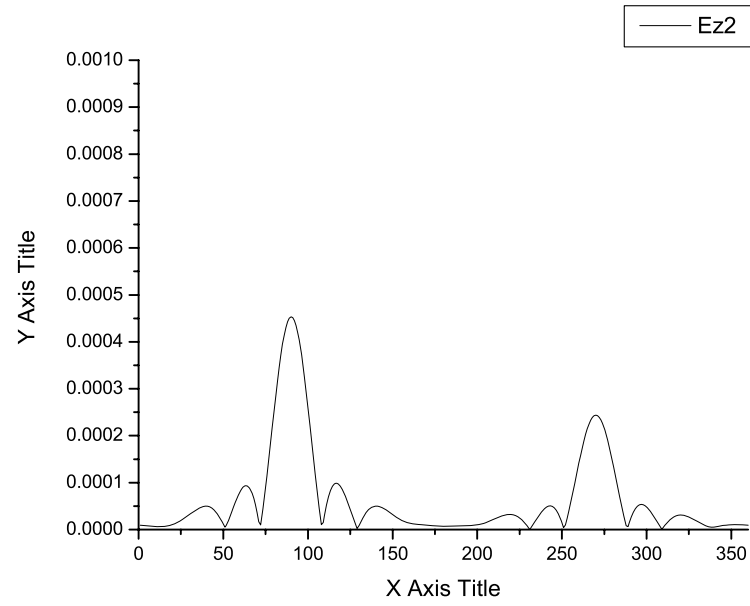


Figure 3.17:  $E_z$  of the slab of case < 2 > at 15.8 GHz when  $\varepsilon = 2.40 - 0.20j$

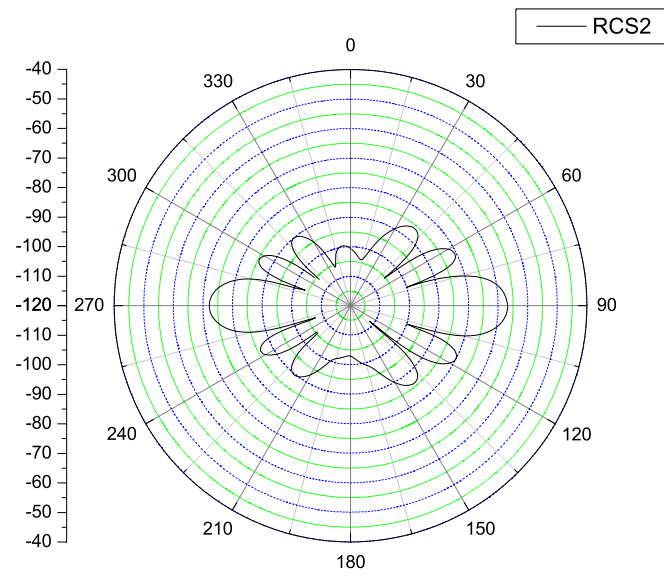


Figure 3.18: RCS of the slab of case < 2 > at 15.8 GHz when  $\varepsilon = 2.40 - 0.20j$

### 3.4 Conclusion for AIM Algorithm

The structures of SRR with wires behave as a magnetic conductor in the vicinity of resonant frequency. By applying the fast solver AIM, the CPU time per iteration as well as memory requirement is greatly reduced. Even though some very expensive EM softwares can calculate RCS and  $E_z$  for small scale problems, they are not capable in simulating large problems such as SRR slab. SRR structures are often electrically small but have a large number of unknowns, so AIM is especially suitable to analyze such kind of LHMs. And, since SRR is composed of dielectric body and metal surface, we introduce both volume and surface into our program. After a rough validation of the code, we first use a few inclusions to find the resonant frequency, then at the vicinity of this frequency, an SRR slab is tested when the illuminator are two different plane waves while only the first one can induce magnetic resonance. We find that when the magnetic resonance is achieved, most power can be transferred to the other side of the slab which satisfies the property of LHM. However, when there is no magnetic resonance, most power will not be able to go through the slab. Then we change the permittivity of dielectric volume to observe its effect on scattered field. The result prove that we achieve high precision with the lowest memory and CPU time cost, and that our algorithm is efficient enough for any composite LHM design and simulation.

## Chapter 4

# Application of Left-handed Material with New Designs

### 4.1 Microstrip Lines Loaded With Flower-shaped Left-handed Resonators

#### 4.1.1 Introduction of Microstrip Lines Loaded with CSRR and Capatitors

In this work, microstrip lines loaded with flower-shaped left-handed resonators and series interdigital capacitors are modeled by means of a lumped element equivalent circuit. The structures exhibit a left-handed (or backward wave) behavior at a relatively broad frequency range. That is a huge improvement to the conventional SRR structure which has very narrow bandwidth and high loss. Also, we explored the equivalent circuit at the left-handed frequency. The equivalent circuit model is able to accurately describe the frequency responses of the structures in the left-handed transmission band, the forbidden band, and the lower frequency region of the forward allowed band. The limitations of this circuit model to properly predict the behavior of the structures at higher frequencies (mainly related to the Bragg effect caused by periodicity) are pointed out.

Complementary split rings resonators (CSRRs) have been recently proposed by some of the authors of this manuscript as new resonant constitutive elements for the synthesis of negative permittivity metamaterials [43]. By combining these resonators with series capacitive gaps, one-dimensional left-handed structures were implemented in microstrip technology [44]. The required negative value of the effective permeability to achieve left-handedness was due to the presence of the series gaps, which make the structure to behave as a magnetic plasma, with negative value of permeability up to a cutoff (or plasma) frequency. The frequency response of CSRR/gap-loaded microstrip lines exhibits a left-handed (or backward wave) transmission band in that region where negative permeability and permittivity simultaneously coexist, and this typically occurs in a narrow (or moderate) band below the plasma frequency of the gap-related structure, i.e. in the vicinity of the resonance frequency of CSRRs [44]. Above this band, the effective permittivity changes sign and signal propagation is inhibited. However, above the plasma frequency also the effective permeability of the artificial line switches to a positive value, and signal propagation is allowed,

although wave transmission is forward, rather than backward. Thus, the typical behavior of these resonant type left-handed lines is indeed similar to that of the so-called composite right-/left-handed (CRLH) transmission lines, where a left-handed and a right-handed transmission bands, separated by a frequency gap, are present [19]. In CRLH lines, the left-handed band, at lower frequencies, is due to the presence of series gaps and shunt stubs loading the line, whereas forward wave transmission is related to the parasitic elements of the host line. To properly model the behavior of CSRR-based left-handed microstrip lines, a lumped element equivalent circuit model has been previously proposed [45]. This model has been found to describe the frequency response in the left-handed band to a good approximation. And the capability of the model to also predict transmission line behavior above that band is explored by [46].

### 4.1.2 The Novel Planar Negative Refractive Index Structure

A novel 2D planar distributed NRI structure which is very likely the performance of CSRR, is proposed previously by Naoko Natrunaga etc [47]. The structure consists of a 2D periodic array of unit cells with metal patterns on the both sides of a substrate and it does not require any vias. Without vias, is the structure scalable to millimeter-wave frequency range or above. It is also advantageous that the structure can be fabricated by using conventional MMIC processes. The structure were experimentally verified of the left-handed characteristics.

The structure is the planar structure with metal patterns on both the upper and lower layers of the substrate as shown in Figure 4.1(a) and (b), respectively. Let us consider a square unit cell with the period  $a$  in both the  $x$  and  $y$  directions for simplicity. The unit cell is depicted with the dotted line in Figure 4.1(a) and (b). On the upper layer, are the 45-degree rotated square metal patches with the sides. On the lower layer, four isosceles triangles surrounded by a square frame are connected at their apex, and from the connected portion, four narrow metal strips are radially connected to the outer frame in the unit cell. The upper layer pattern lies on the lower layer pattern with the relation shown in 4.1(c). The upper metal patch overlaps the isosceles triangles forming an MIM capacitor, which provides a large series capacitance between the adjacent unit cells and a frequency band of negative  $\epsilon$ . The four radial strips bridge the series capacitor and the outer frame. When the area of the outer frame is large enough and has a quasi-ground voltage, the bridging strips work as shunt inductances and can provide negative  $\mu$  at a frequency band. When the series capacitance and the shunt inductance are large enough, in other words, the negative  $\epsilon$  and negative  $\mu$  appear at the same frequency band, the structure is verified that it can work as a left-handed structure during a particular frequency [47].

However, before utilizing the structure in microstrip line, we find the bandwidth of such structure as shown in Fig 4.2 can be further improved by the changing the shape of isosceles triangles into the flower-shape strip as shown in 4.3. To prove with this shape can obtain better performance, we etch these two structures into the ground plane of a microstrip line to see the transmission ability vs frequency. As we stated before, the isosceles triangle can provide negative  $\mu$  in a frequency band which will be stopband if we want to observe the  $S_{21}$  of these microstrip lines.

After we examined the stop-band of the structures shown in Figure 4.2 and Figure 4.3. The stop-band for the original triangle structure is from 7-8GHz as shown in Figure 4.4, while the modified flower structure's stop-band is from 8.8-10.6GHz as shown in Figure 4.5. So we add

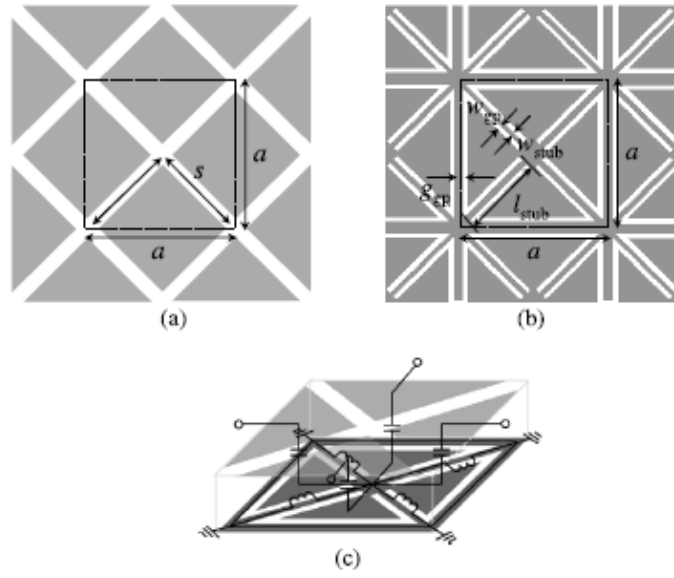


Figure 4.1: Proposed 2D NRI structure. (a) Upper layer. (b) Lower layer. (c) Unit cell.

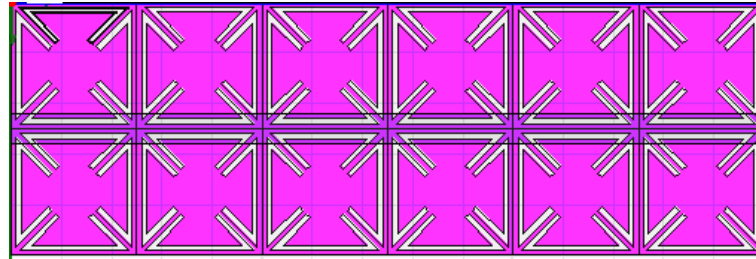


Figure 4.2: Top view of a microstrip line with 2 rows of triangle-shaped left-handed pattern on the ground plane

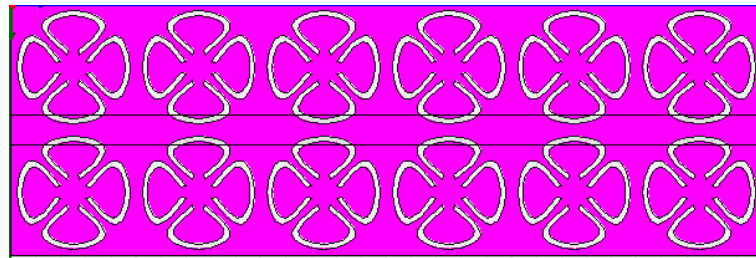


Figure 4.3: Top view of a microstrip line with 2 rows of flower-shaped left-handed pattern on the ground plane

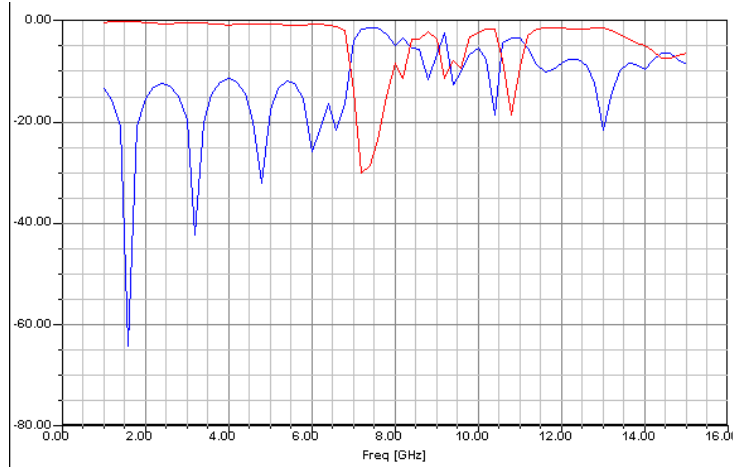


Figure 4.4: S-parameter of a microstrip line with 2 row of triangle-shape left-handed pattern on the ground plane and interdigital capacitors on the stripline (red line represents  $S_{21}$  and blue line represents  $S_{11}$ )

capacitor onto the microstrip line (Figure 4.6 and Figure 4.7), which finally provide a C-L circuit and induce both negative  $\mu$  and negative  $\epsilon$ . Now the stop-band becomes a pass-band, and most important, the pass-band is as wide as 2.5GHz as shown in Figure 4.8.

## 4.2 Microstrip-feed Patch Antenna with Left-handed Elements

### 4.2.1 Novel Patch Antenna with LH Element and Its Performance

In this section, we apply the triangle structure into the fabrication of patch antenna. The model we designed is shown in Figure 4.9 and Figure 4.10. And the  $S_{11}$  of the proposed antenna is shown in Figure 4.11. We can see that the bandwidth is from 5.1-9.2GHz. The VSWR is shown in Figure 4.12. Obviously, during the working band, the VSWR is effectively suppressed below 2. The 3D radiation pattern at 7GHz and 8.1GHz is depicted in Figure 4.14 and Figure 4.15 respectively. We can see that the radiation is mainly gathering at the direction of  $\theta = 90^\circ, \phi = 90^\circ$  which is quite different from a traditional patch antenna's main radiation direction ( $\theta = 0^\circ$ ). This can be explained by the transmission of backward wave from the feed line to the end of the substrate.

At the frequency of 7GHz, on  $\theta = 90^\circ$  plane, as shown in Figure 4.16, the main lobe magnitude of the antenna is 4.9dBi. The main lobe direction is at  $\phi = 105^\circ$  and the angular width (3dB) is  $67.1^\circ$ . The side lobe level is  $-3.5$ dB.

At the frequency of 8.1GHz, on  $\theta = 90^\circ$  plane, as shown in Figure 4.17, the main lobe magnitude of the antenna is 6.3dBi. The main lobe direction is at  $\phi = 100^\circ$  and the angular width (3dB) is  $57.2^\circ$ . The side lobe level is  $-4.8$ dB.

At the frequency of 7GHz, on  $\phi = 90^\circ$  plane, as shown in Figure 4.18, the main lobe magnitude of the antenna is 4.2dBi, which is quite favorable for a single patch antenna. the main lobe direction is at  $\phi = 80^\circ$  and the angular width (3dB) is  $142.8^\circ$ .

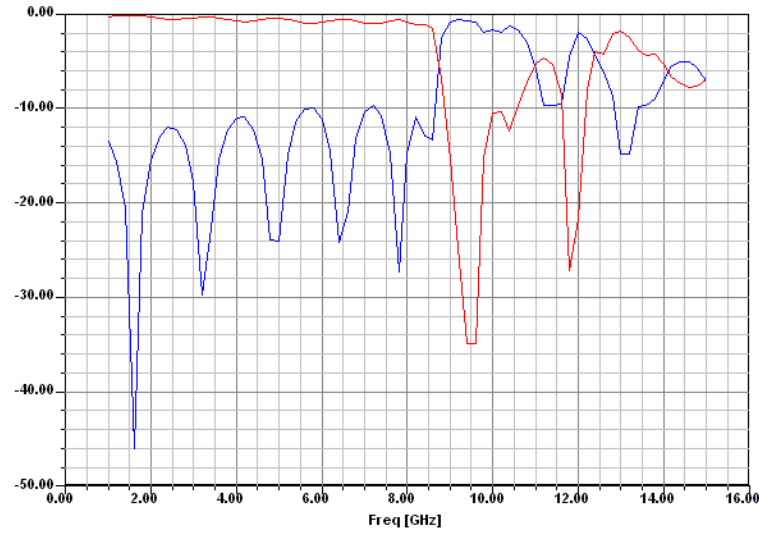


Figure 4.5: S-parameter of a microstrip line with 2 row of flower-shape left-handed pattern etched on the ground plane and interdigital capacitors on the stripline (red line represents  $S_{21}$  and blue line represents  $S_{11}$ )

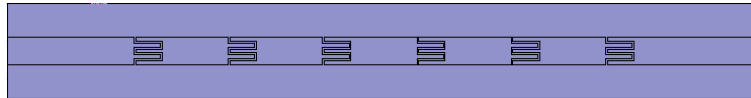


Figure 4.6: Top view of a microstrip line with 1 row of flower-shape left-handed pattern on the ground plane and interdigital capacitors on the stripline



Figure 4.7: Bottom view of a microstrip line with 1 row of flower-shape left-handed pattern on the ground plane and interdigital capacitors on the stripline

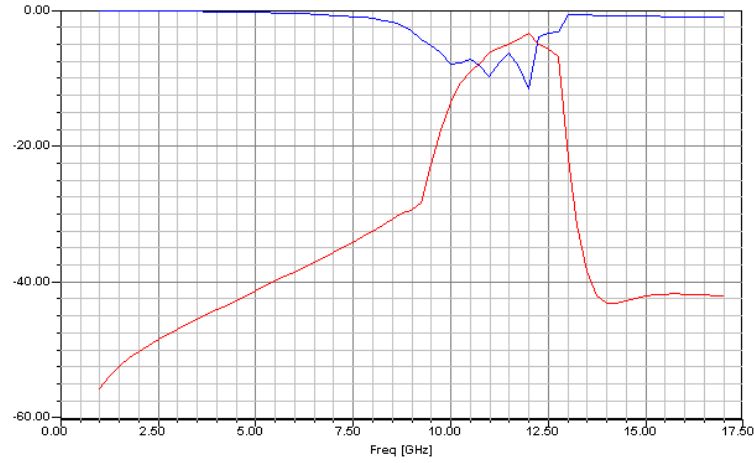


Figure 4.8: S-parameter of a microstrip line with 1 row of flower-shape left-handed pattern etched on the ground plane and interdigital capacitors on the stripline (red line represents  $S_{21}$  and blue line represents  $S_{11}$ )

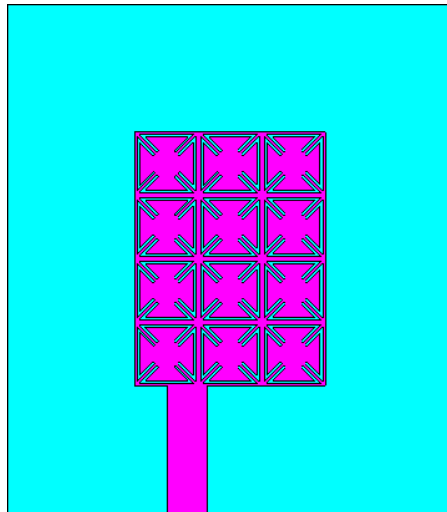


Figure 4.9: Top view of the simulated antenna (blue part is substrate while pink part shows metal surface)



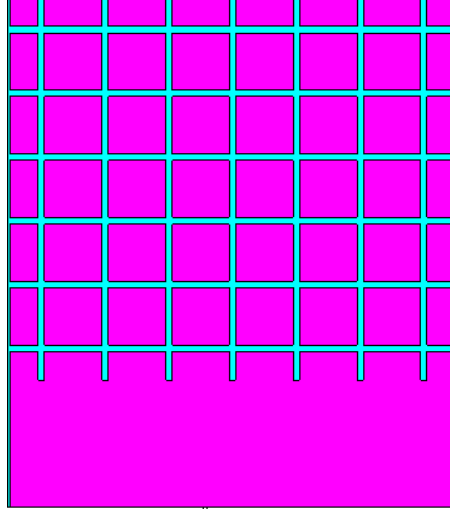


Figure 4.10: Bottom view of the simulated antenna (blue part is substrate while pink part shows metal surface)

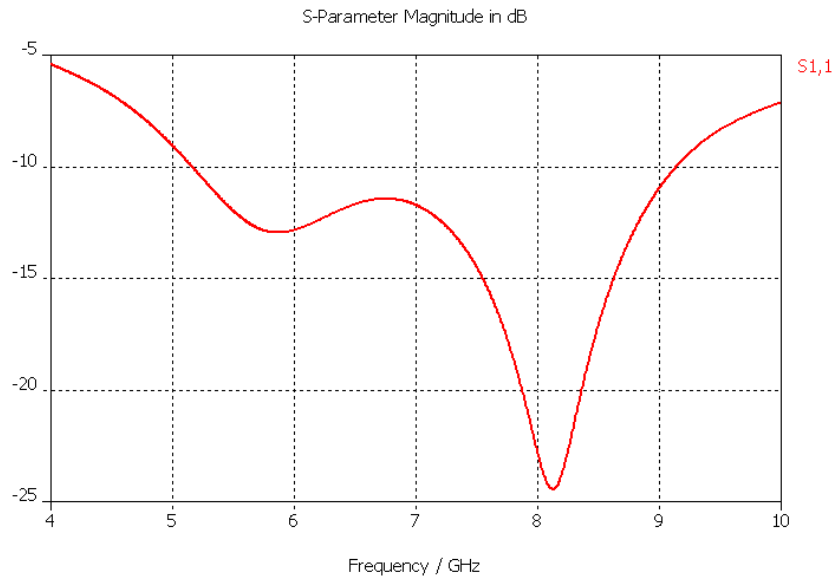


Figure 4.11: Simulated  $S_{11}$  against frequency of patch antenna with triangle shaped gaps on patch and strip bridges on ground

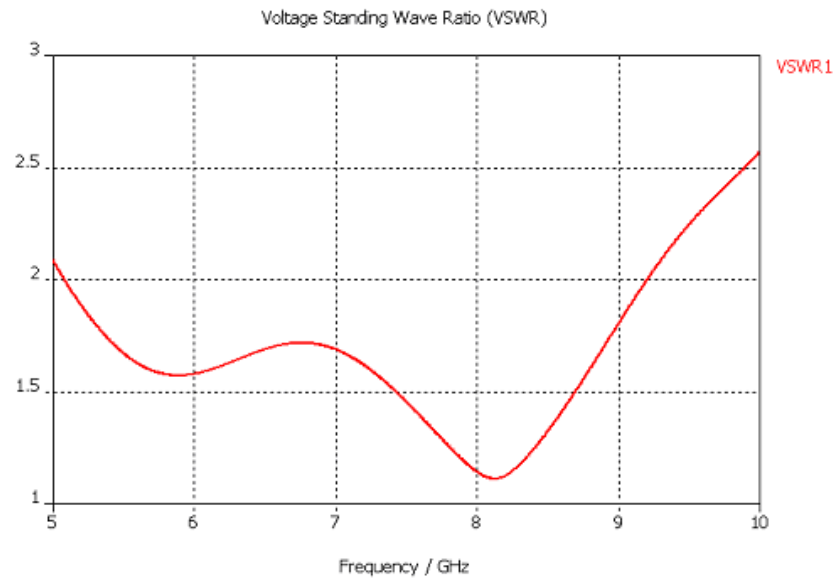


Figure 4.12: Simulated VSWR against frequency of patch antenna with triangle shaped gaps on patch and strip bridges on ground

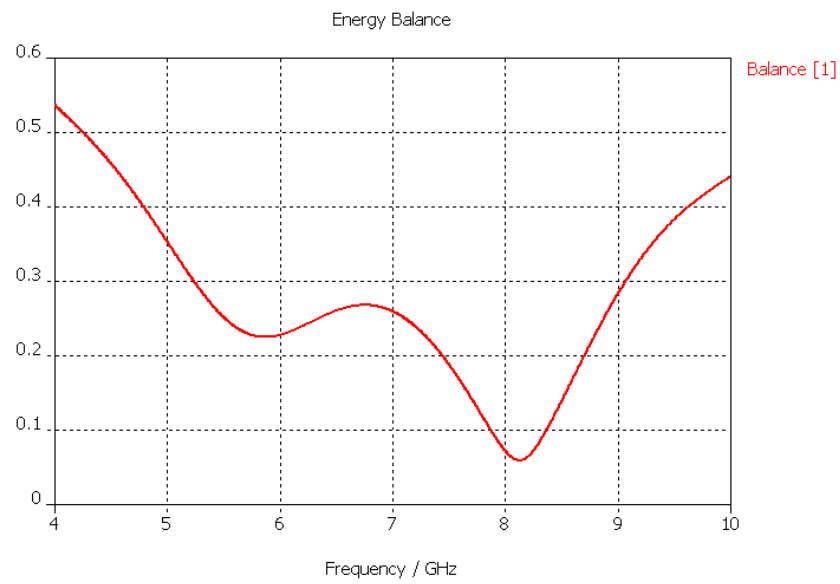


Figure 4.13: Simulated antenna balance vs frequency in the working band

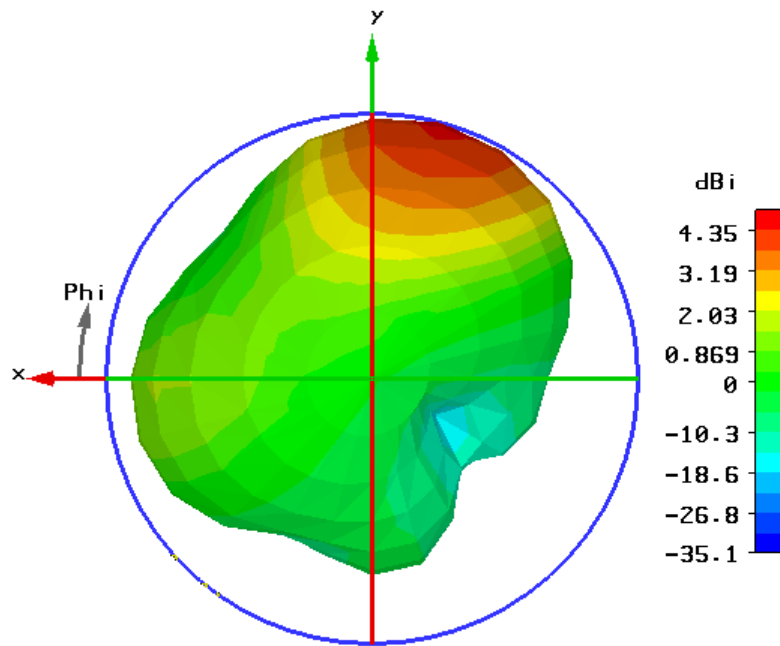


Figure 4.14: Simulated 3D radiation pattern at the frequency of 7GHz

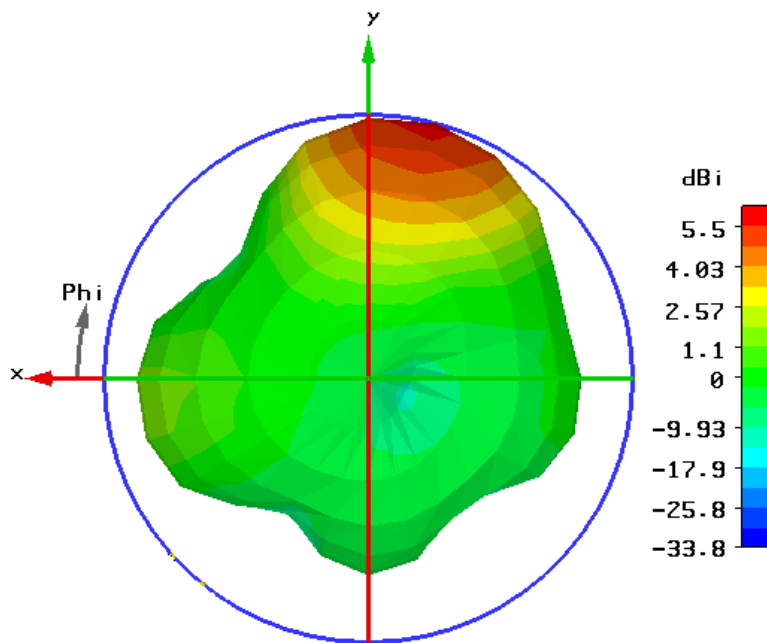
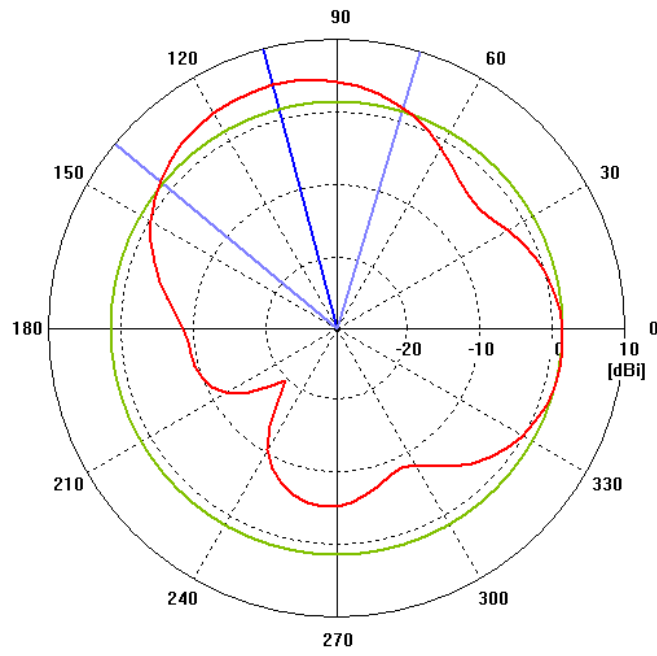
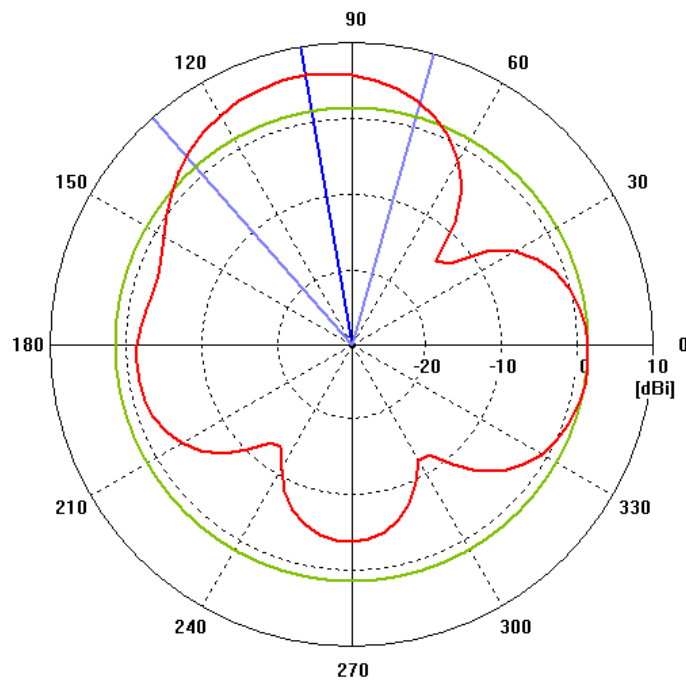


Figure 4.15: Simulated 3D radiation pattern at the frequency of 8.1GHz

Figure 4.16: Simulated radiation pattern at 7GHz on the plane of  $\theta = 90^\circ$ Figure 4.17: Simulated radiation pattern at 8.1GHz on the plane of  $\theta = 90^\circ$

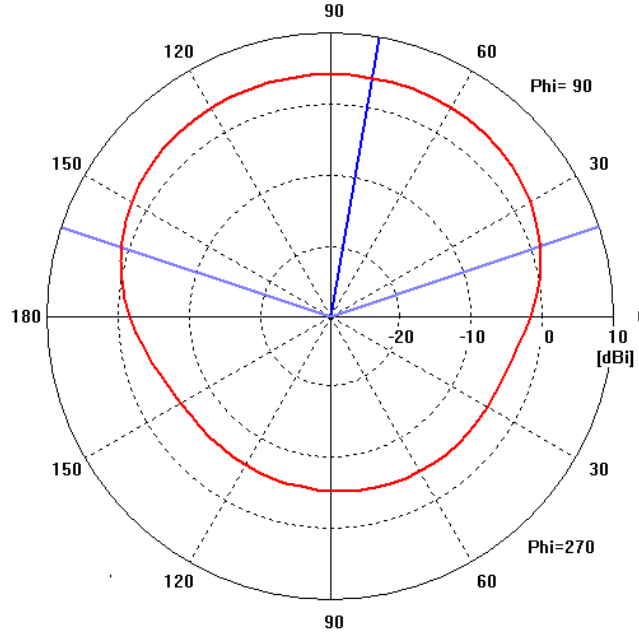


Figure 4.18: Simulated radiation pattern at 7GHz on the plane of  $\phi = 90^\circ$

At the frequency of 8.1GHz, on  $\phi = 90^\circ$  plane, as shown in Figure 4.19, the main lobe magnitude of the antenna is 5.8dBi. The main lobe direction is at  $\theta = 90^\circ$  and the angular width (3dB) is  $114.4^\circ$ . The side lobe level is about  $-7.6$ dB.

#### 4.2.2 Conclusion for the Application

We fabricated the patch antenna as shown in Figure 4.20 and Figure 4.21 with left-handed patterns and gaps etched on the patch and ground plane respectively. We find a good agreement between the experimental results and the simulation prediction. This antenna overcome the disadvantage of traditional patch antenna's narrow bandwidth by enhance the radiation with left-handed element we present in the previous sections. The radiation efficiency is very high, which shows most energy is radiated rather than wasted thermally. At the mean time, the gain of such LH-enhanced antenna is high, and the side lobes are well suppressed.

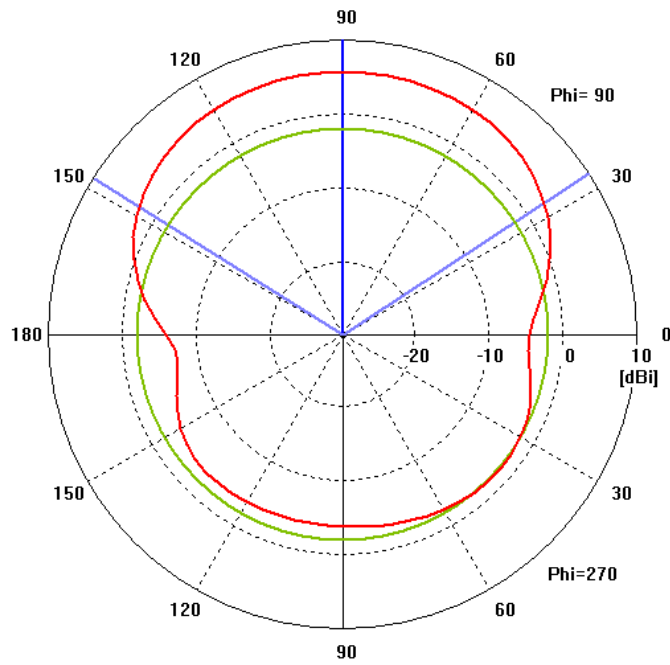


Figure 4.19: Simulated radiation pattern at 8.1GHz on the plane of  $\phi = 90^\circ$

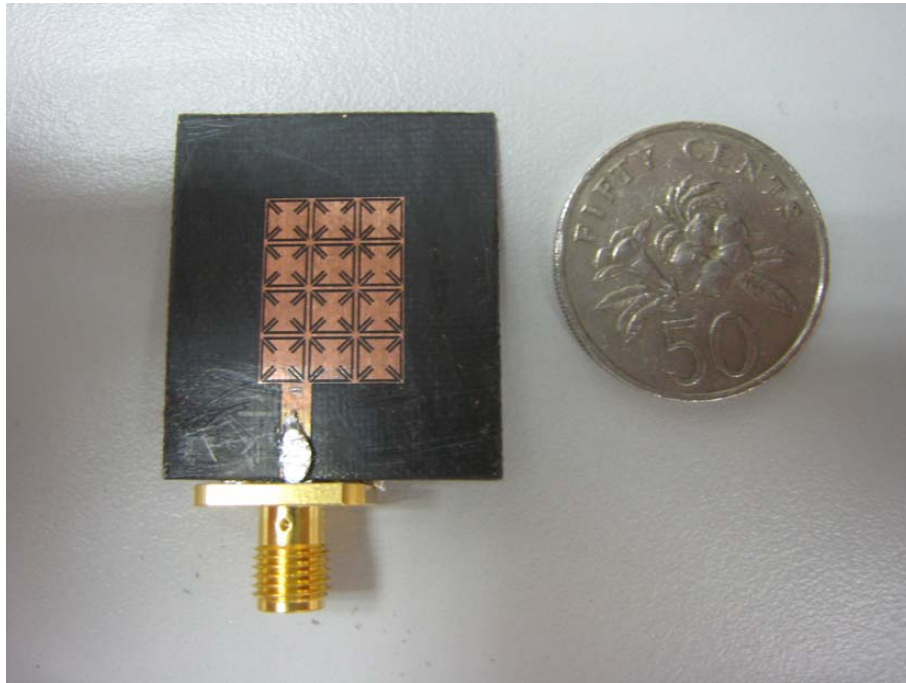


Figure 4.20: Top view of the fabricated antenna ( $\epsilon=2.2$ , substrate thickness  $h=0.794\text{mm}$ , substrate size= $28.1\text{mm} \times 32\text{mm}$ , patch size= $12\text{mm} \times 16\text{mm}$ )

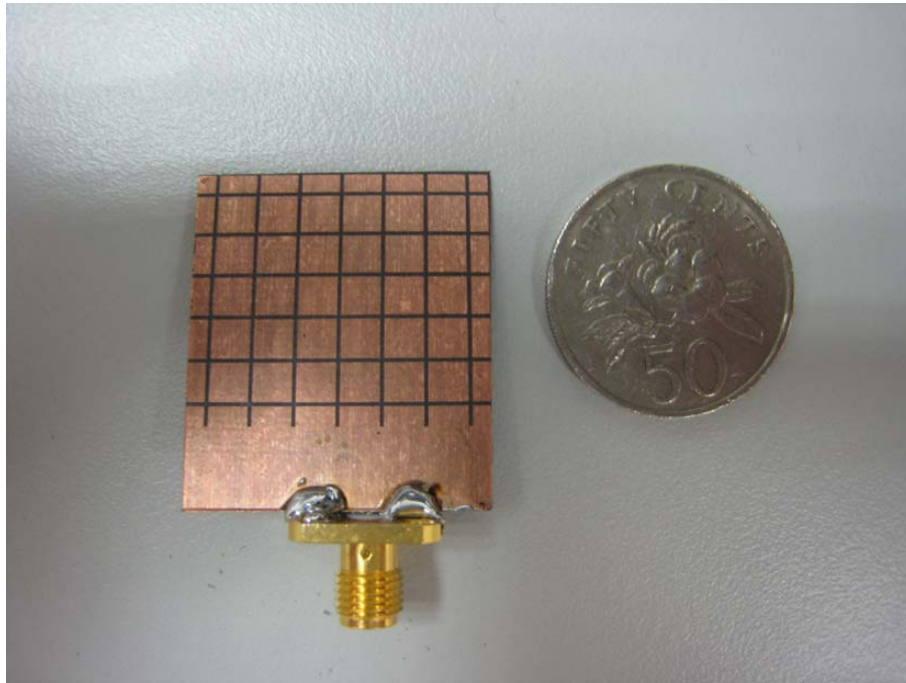


Figure 4.21: Bottom view of the fabricated antenna (width of gaps=0.4mm)

## Chapter 5

# Proposed Future Research Topics

Base on previous result, we can see an obvious pass band of the SRR slab. To be more convincing, we are going to show more LH property of this SRR structure such as the negative refractive index.

In our future work, we plan to build a SRR prism as shown in Figure 5.2 and Figure 5.3. We can use the devices shown in Figure 5.1 to measure the angle of refraction. The prism we design still uses the basic SRR element shown in Figure 3.2. The whole prism is shown in Figure 5.2 and Figure 5.3. This model is built and meshed in FEKO 5.0 which require 9G memory to apply traditional MoM. However, with our AIM algorithm, it is estimated that only 2G memory is required.

With this structure, we are expecting to observe an obvious negative refraction from the prism. If this simulation can be performed successfully, we will go on with the implementation of our code. For example, we will adopt periodic Green's function to further reduce computation complexity. As for the design of antenna, we can also include multi-layer Green's function to enhance the accuracy as well as the computation speed of the code [48][49]. Because a full-wave Greens function completely define the field inside a multi-layer dielectric structure due to a current element arbitrarily placed between any two layers in two-dimensional spectral-domain form. It is derived by solving a "standard" form containing the current element with two substrates on either side of it, and using an iterative algorithm to take care of additional layers. Another iterative algorithm is then used to find the field in any layer in terms of the field expressions in the two layers of the "standard" form.

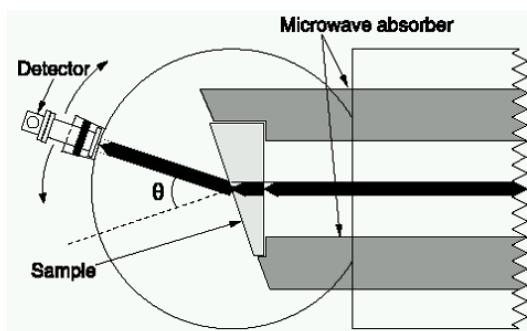


Figure 5.1: Special device for measurements of angles of refractions



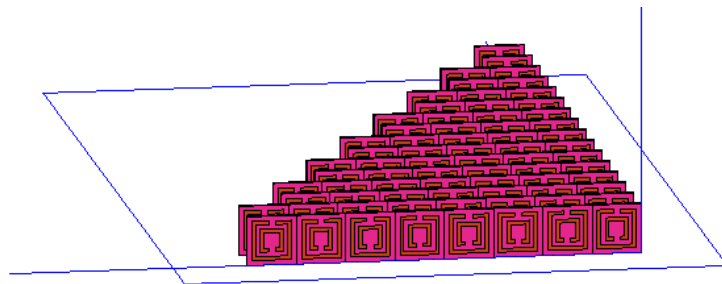


Figure 5.2: 3D view of SRR prism



Figure 5.3: Top view of SRR prism

The locations of the poles of the Greens function can be predicted. Higher order interpolatory basis functions defined on curvilinear triangular patches also can be used to provide necessary flexibility and accuracy for the discretization of arbitrary shapes and to offer a better convergence than lower order basis functions. The combination of the improved DCIM and the higher order basis functions results in an efficient and accurate MoM analysis for 3-D multi-layer microstrip structures. So this kind of Green's function can be applied to a few multilayer transmission or radiation structures. After all these work, our algorithm will become an even more powerful numerical simulation tool.

As to the design of new left-handed structure and application aspect, we can first extent the LH-enhanced patch antenna into antenna array and see what further improvement can be made. Then we can adopt various structures discovered with LH characteristics into a large variety of devices such as microstrip filter, power divider, coupler [50] as well as antenna fabrication [51]. Many theoretical predictions and new LH patterns design have been done to serve the application. However, to date, the design and fabrication of practical devices is still mainly based on the traditional SRR or  $\Omega$  structure which has extremely high loss and narrow bandwidth. To open a new world of LHM application, we are going to make better use of current research result and try to explore various practical applications.

# Appendix A

## Useful Formulations

### A.1 RWG Basis Function – Triangular Modeling Method for Surface Element

#### A.1.1 Development of RWG Basis Function

Let  $S$  denote the surface of an open or closed perfectly conducting scatterer. SWG is the short for Rao-Wilton-Glisson basis function. Each basis function is associated with a interior edge (i.e., nonboundary edge ) of the patch model and is to vanish everywhere on  $S$  except in the two triangles attached to that edge. Figure A.1 shows two such triangles,  $T_n^+$  and  $T_n^-$ , corresponding to the  $n$ th edge of triangulated surface modeling a scatterer. Points in  $T_n^+$  may be designated either by the position vector  $\mathbf{r}$  defined with respect to  $O$ , or by the free vertex of  $T_n^+$ . Similar remarks apply to the position vector  $\rho_n^-$  except that it is directed toward the free vertex of  $T_n^-$ . The plus or minus designation of the triangles is determined by the choice of a positive current reference direction for the  $n$ th edge, the reference for which is assumed to be from  $T_n^+$  to  $T_n^-$ . We define the vector basis function associated with the  $n$ th edge as

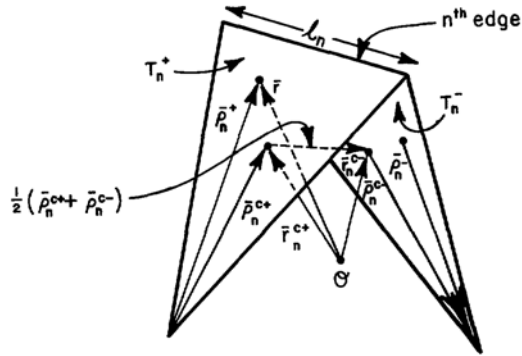


Figure A.1: Triangle pair and geometrical parameters associated with interior edge

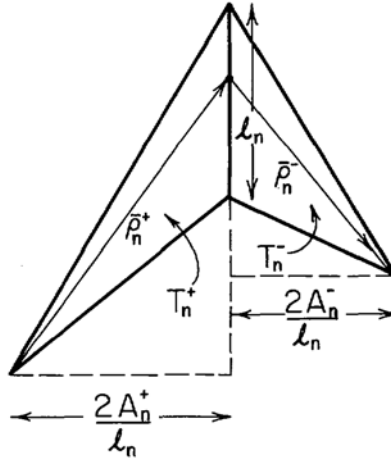


Figure A.2: Geometry for construction of component of basis function normal to edge

$$\mathbf{f}_n(\mathbf{r}) = \begin{cases} \frac{l_n}{2A_n^+} \rho_n^+, & \mathbf{r} \in T_n^+; \\ \frac{l_n}{2A_n^-} \rho_n^-, & \mathbf{r} \in T_n^-; \\ 0, & \text{otherwise.} \end{cases} \quad (\text{A.1})$$

where  $l_n$  is the length of the edge and  $A_n^\pm$  is the area of triangle  $T_n^\pm$ . (Note that we use the convention, followed throughout the report, that subscripts refer to edges while superscripts refer to faces.) The basis function  $\mathbf{f}_n$  is used to approximately represent the surface current, and we list and discuss below some properties which make it uniquely suited to this role.

1) The current has no component normal to the boundary (which excludes the common edge) of the surface formed by the triangle pair  $T_n^+$  and  $T_n^-$ , and hence no line charges exist along this boundary.

2) The component of current normal to the  $n$ th edge is constant and continuous across the edge as may be seen with the aid of Figure A.2, which shows that the normal component of  $\rho_n^\pm$  along edge  $n$  is just the height of triangle  $T_n^\pm$  with edge  $n$  as the base and the height expressed as  $(2A_n^\pm)/l_n$ . This latter factor normalizes  $\mathbf{f}_n$  in such that its flux density normal to edge  $n$  is unity, ensuring continuity of current normal to the edge. This result, together with 1), implies that all edges of  $T_n^+$  and  $T_n^-$  are free of line charges.

3) The surface divergence of  $\mathbf{f}_n$ , which is proportional to the surface charge density associated with the basis element, is

$$\nabla_s \cdot \mathbf{f}_n(\mathbf{r}) = \begin{cases} \frac{l_n}{A_n^+}, & \mathbf{r} \in T_n^+, \\ -\frac{l_n}{A_n^-}, & \mathbf{r} \in T_n^-, \\ 0, & \text{otherwise.} \end{cases} \quad (\text{A.2})$$

since the surface divergence in  $T_n^\pm$  is  $\frac{\pm 1}{\rho_n^\pm} \frac{\partial[\pm(\rho_n^\pm)^2 f_n]}{\partial \rho_n^\pm}$ . The charge density is thus constant in each triangle, the total charge associated with the triangle pair  $T_n^+$  and  $T_n^-$  is zero, and the basis functions for the charge evidently have the form of pulse doublets.

4) The moment of  $\mathbf{f}_n$  is given by  $(A_n^+ + A_n^-)\mathbf{f}_n^{avg}$  where

$$\begin{aligned} (A_n^+ + A_n^-)\mathbf{f}_n^{avg} &\equiv \int_{T_n^+ + T_n^-} \mathbf{f}_n dS \\ &= \frac{l_n}{2}(\rho_n^{c+} + \rho_n^{c-}) \\ &= l_n(r_n^{c+} + r_n^{c-}) \end{aligned} \quad (\text{A.3})$$

and  $\rho_n^{c\pm}$  is the vector between the free vertex and the centroid of  $T_n^\pm$  with  $\rho_n^{c-}$  directed toward and  $\rho_n^{c+}$  directed away from the vertex, as shown in Figure A.1, and  $r_n^{c\pm}$  is the vector from  $O$  to the centroid of  $T_n^\pm$ . (A.3) may be most easily derived by expressing the integral in terms of area coordinates, to be discussed below.

The current on  $S$  may be approximated in terms of the  $\mathbf{f}_n$ , as

$$J \cong \sum_{n=1}^N I_n \mathbf{f}_n(\mathbf{r}) \quad (\text{A.4})$$

where  $N$  is the number of interior (nonboundary) edges. Since a basis function is associated with each nonboundary edge of the triangulated structure, up to three basis functions may have nonzero values within each triangular face. But at a given edge only the basis function associated with that edge has a current component normal to the edge since, according to 1), all other basis currents in adjacent faces are parallel to the edge. Furthermore, since the normal component of  $\mathbf{f}_n$  at the  $n$ th edge is unity, each coefficient  $I_n$ , in (A.4) may be interpreted as the normal component of current density flowing past the  $n$ th edge. Also, we see that the basis functions are independent in each triangle since the current normal to the  $n$ th edge,  $I_n$  in (A.4), is an independent quantity. At surface boundary edges, the sum of the normal components of current on opposite sides of the surface cancel because of current continuity. Therefore we neither define nor include in (A.4) contributions from basis functions associated with such edges. Because of the considerable variation in the direction of the flow lines of  $\mathbf{f}_n$  within a triangle, it is not at first obvious that a linear superposition of basis functions is capable of representing, say, a constant current flowing in an arbitrary direction within a triangle. That this is possible, however, can be seen with the aid of Figure A.3, which shows a triangle  $T^q$  with edges arbitrarily labeled 1, 2, and 3 (in effect, we employ here a local indexing scheme, in contrast to the global indexing scheme used earlier). With the vectors  $\rho_1$ ,  $\rho_2$  and  $\rho_3$  as shown, the basis functions in  $T^q$  are  $\mathbf{f}_i = (l_i/2A^q)\rho_i$ ,  $i = 1, 2, 3$ , where  $A^q$  is the triangle area and where, for simplicity, the current reference directions are assumed to be out of the triangle for each edge. It is apparent from the figure and the definition of  $\mathbf{f}_i$  that the linear combinations  $l_2\mathbf{f}_1 - l_1\mathbf{f}_2$  and  $l_3\mathbf{f}_1 - l_1\mathbf{f}_3$  are constant vectors for every point  $\mathbf{r}$  in  $T^q$  and are parallel to sides 3 and 2, respectively. Since the two composite forms are linearly independent (i.e., nonparallel), a constant vector of arbitrary magnitude and direction within  $T^q$  may be synthesized by an appropriate linear combination of the two forms, as asserted.

### A.1.2 Testing Procedure of RWG Basis Function

The next step in the method of moments is to select a testing procedure. We choose as testing functions the expansion functions  $\mathbf{f}_n$ , developed in the previous section. With a symmetric product defined as



be written as

$$\begin{aligned}
& \left\langle \left\{ \begin{array}{c} \mathbf{E}^{inc} \\ \mathbf{A} \end{array} \right\}, \mathbf{f}_m \right\rangle \\
&= l_m \left[ \frac{1}{2A_m^+} \int_{T_m^+} \left\{ \begin{array}{c} \mathbf{E}^{inc} \\ \mathbf{A} \end{array} \right\} \cdot \rho_m^+ dS + \frac{1}{2A_m^-} \int_{T_m^-} \left\{ \begin{array}{c} \mathbf{E}^{inc} \\ \mathbf{A} \end{array} \right\} \cdot \rho_m^- dS \right] \\
&\cong \frac{l_m}{2} \left[ \left\{ \begin{array}{c} \mathbf{E}^{inc}(\mathbf{r}_m^{c+}) \\ \mathbf{A}(\mathbf{r}_m^{c+}) \end{array} \right\} \cdot \rho_m^{c+} + \left\{ \begin{array}{c} \mathbf{E}^{inc}(\mathbf{r}_m^{c-}) \\ \mathbf{A}(\mathbf{r}_m^{c-}) \end{array} \right\} \cdot \rho_m^{c-} \right] \tag{A.10}
\end{aligned}$$

where the integral over each triangle is eliminated by approximating  $\mathbf{E}^{inc}$  (or  $\mathbf{A}$ ) in each triangle by its value at the triangle centroid and carrying out integrations similar to those used to obtain (A.3). With (A.2 A.9 A.10), (A.7) now becomes:

$$\begin{aligned}
& j\omega l_m \left[ \mathbf{A}(\mathbf{r}_m^{c+}) \cdot \frac{\rho_m^{c+}}{2} + \mathbf{A}(\mathbf{r}_m^{c-}) \cdot \frac{\rho_m^{c-}}{2} \right] + l_m [\Phi(\mathbf{r}_m^{c-}) - \Phi(\mathbf{r}_m^{c+})] \\
&= l_m \left[ \mathbf{E}^{inc}(\mathbf{r}_m^{c+}) \cdot \frac{\rho_m^{c+}}{2} + \mathbf{E}^{inc}(\mathbf{r}_m^{c-}) \cdot \frac{\rho_m^{c-}}{2} \right] \tag{A.11}
\end{aligned}$$

which is the equation enforced at each triangle edge,  $m = 1, 2, \dots, N$ .

We remark that another interpretation of the testing procedure arriving at A.11 is also possible. One may equate line integrals of the form  $\int_{C_m} \mathbf{F} \cdot d\mathbf{r}$ , where  $\mathbf{F}$  represents the right and left sides of (A.6), and  $C_m$  is the piecewise linear path from the point  $\mathbf{r}_m^{c+}$  to the midpoint of edge  $m$  and thence to  $\mathbf{r}_m^{c-}$ .  $\mathbf{E}^{inc}$  and  $\mathbf{A}$  can be approximated along each portion of the path by their respective values at the triangle centroids. The resulting equality, apart from the factor  $l_m$ , is (A.11). Under either interpretation, the testing procedure reduces the differentiability requirement on  $\Phi$  in (A.6) by integrating  $\nabla\Phi$  first, the procedure having been constructed with this goal in mind. The purpose of approximations (A.9) and (A.10) is to eliminate surface integrals of the potential quantities, allowing a double surface integral to be approximated by a quantity involving a single surface integral in the numerical computation of the moment matrix elements. These approximations are justified by observing that the potentials are locally smooth within each subdomain, as follows from their integral definitions and the locally smooth nature of the source representation in terms of the basis functions.

### A.1.3 Elements of the Matrix and Excitation Vector of RWG

Substitution of the current expansion (A.4) into (A.11) yields an  $N \times N$  system of linear equations which may be written in matrix form as

$$ZI = V \tag{A.12}$$

where  $Z = [Z_{mn}]$  is an  $N \times N$  matrix and  $I = [I_n]$  and  $V = [V_m]$  are column vectors of length  $N$ . Elements of  $Z$  and  $V$  are given by

$$Z_{mn} = l_m \left[ j\omega \left( \mathbf{A}_{mn}^+ \cdot \frac{\rho_m^{c+}}{2} + \mathbf{A}_{mn}^- \cdot \frac{\rho_m^{c-}}{2} \right) + \Phi_{mn}^- - \Phi_{mn}^+ \right] \tag{A.13}$$

$$V_m = l_m \left( \mathbf{E}_m^+ \cdot \frac{\rho_m^{c+}}{2} + \mathbf{E}_m^- \cdot \frac{\rho_m^{c-}}{2} \right) \quad (\text{A.14})$$

where

$$\mathbf{A}_{mn}^\pm = \frac{\mu}{4\pi} \int_S \mathbf{f}_n(\mathbf{r}') \frac{e^{-jkR_m^\pm}}{R_m^\pm} dS' \quad (\text{A.15})$$

$$\Phi_{mn}^\pm = -\frac{1}{4\pi j\omega\varepsilon} \int_S \nabla'_S \cdot \mathbf{f}_n(\mathbf{r}') \frac{e^{-jkR_m^\pm}}{R_m^\pm} dS' \quad (\text{A.16})$$

$$R_m^\pm = |\mathbf{r}_m^{c\pm} - \mathbf{r}'| \quad (\text{A.17})$$

and

$$\mathbf{E}_m^\pm = \mathbf{E}^{inc}(\mathbf{r}_m^{c\pm}) \quad (\text{A.18})$$

For plane wave incidence, we set

$$\mathbf{E}_i(\mathbf{r}) = (E_\theta \hat{\theta}_0 + E_\phi \hat{\phi}_0) e^{j\mathbf{k} \cdot \mathbf{r}} \quad (\text{A.19})$$

where the propagation vector  $\mathbf{k}$  is

$$\mathbf{k} = k(\sin \theta_0 \cos \phi_0 \hat{\mathbf{x}} + \sin \theta_0 \sin \phi_0 \hat{\mathbf{y}} + \cos \theta_0 \hat{\mathbf{z}}) \quad (\text{A.20})$$

and  $(\hat{\theta}_0, \hat{\phi}_0)$  defines the angle of arrival of the plane wave in terms of the usual spherical coordinate convention. Unit vectors  $\theta_0$  and  $\phi_0$  are constant vectors which coincide with the usual spherical coordinate unit vectors only at points on the line from  $O$  in the direction of  $\mathbf{k}$ .

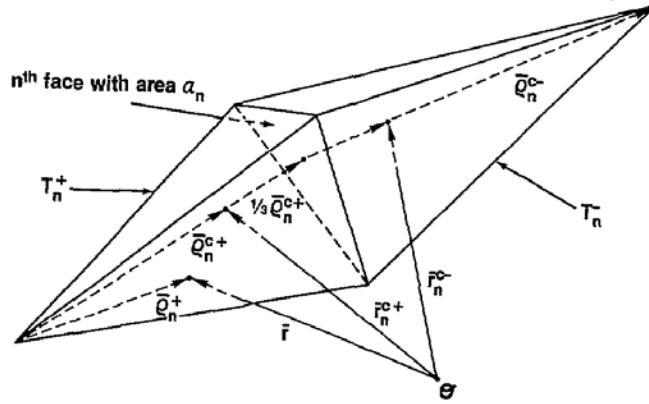
Once the elements of the moment matrix and the forcing vector  $V$  are determined, one may solve the resulting system of linear equations (A.12) for the unknown column vector  $I$ . The elements of  $Z$  in (A.12) may be evaluated by naively computing  $Z_{mn}$  directly by (A.13) (with aid of (A.15) and (A.16)) for each index combination  $m$  and  $n$ . However, as shown in the next section, this procedure is extremely inefficient since the integrals required for each combination of  $m$  and  $n$  are generally required for a number of other combinations as well.

## A.2 SWG Basis Function – Tetrahedral Modeling Method for Volume Element

### A.2.1 Development of SWG Basis Function

The volume  $V$  is assumed to be subdivided into a number of tetrahedral elements such that a homogeneous or inhomogeneous dielectric region is approximated by a number of tetrahedrons, in each of which the dielectric properties are approximated as constant. A homogeneous dielectric




 Figure A.4: Pair of tetrahedrons and geometrical parameters associated with  $n$ th face

region is bounded by a surface that is approximated by triangular faces assigned so as to fit the shape of the surface well.

Once the volume of the scatterer has been appropriately modeled by tetrahedral volumes, the faces of the tetrahedrons are of primary importance for the development of the basis functions. Figure A.4 shows two tetrahedrons  $T_n^+$  and  $T_n^-$ , associated with the  $n$ th face of the subdivided region  $V$  modeling a scatterer. Points in  $T_n^+$  may be designated either by the position vector  $\mathbf{r}$  defined with respect to  $O$ , or by the position vector  $\rho_n^+$  defined with respect to the free vertex of  $T_n^+$ . Similar remarks apply to points in  $T_n^-$  and the position vector  $\rho_n^-$ , except that the latter is directed toward the free vertex of  $T_n^-$ . The plus or minus designation of a tetrahedron is determined by the choice of a positive flux reference direction, which is assumed to be from  $T_n^+$  to  $T_n^-$ . The basis functions that are used for volume part of the moment method solution of (2.15) are such that one basis function is associated with each face of the tetrahedral model of  $V$ . The basis function associated with the  $n$ th face is

$$\mathbf{f}_n(\mathbf{r}) = \begin{cases} \frac{a_n}{3V_n^+} \rho_n^+, & \mathbf{r} \in T_n^+; \\ \frac{a_n}{3V_n^-} \rho_n^-, & \mathbf{r} \in T_n^-; \\ 0, & \text{otherwise.} \end{cases} \quad (\text{A.21})$$

where  $a_n$  is the area of the face and  $V_n^\pm$  is the volume of  $T_n^\pm$ . (Note the convention that subscripts refer to faces while superscripts refer to tetrahedrons.)

The unknown volume electric flux density that enters (2.15) through (2.11,2.13,2.14) can be represented throughout  $V$  by

$$\mathbf{D}(\mathbf{r}) = \sum_{n=1}^N D_n \mathbf{f}_n(\mathbf{r}) \quad (\text{A.22})$$

The summation is over the  $N$  faces that make up the tetrahedral model of  $V$ .

The basis functions  $\mathbf{f}_n(\mathbf{r})$  have several properties that make them useful for representing  $\mathbf{D}(\mathbf{r})$ .

1) Within each tetrahedron  $\mathbf{D}(\mathbf{r})$  is the sum of four linearly independent basis functions (one associated with each face) which can be combined to represent a constant vector in any direction.

2)  $\mathbf{f}_n(\mathbf{r})$  has no component normal to any face except the common face of the conjoined pair  $T_n^+$  and  $T_n^-$ .

3) The component of  $\mathbf{f}_n$  normal to the  $n$ th face is constant and continuous across the face because the normal component of  $\rho_n^\pm$  along face  $n$  is just the height of  $T_n^\pm$  with face  $n$  as the base and the height expressed as  $3V_n^\pm/a_n$ . This latter factor normalizes  $\mathbf{f}_n$  in (A.21) such that its flux density normal to face  $n$  is unity, ensuring continuity of the component of  $\mathbf{f}_n$ , normal to the face.

4) The divergence of the basis function is

$$\nabla \cdot \mathbf{f}_n(\mathbf{r}) = \begin{cases} \frac{a_n}{V_n^+}, & \mathbf{r} \in T_n^+, \\ -\frac{a_n}{V_n^-}, & \mathbf{r} \in T_n^-, \\ 0, & \text{otherwise.} \end{cases} \quad (\text{A.23})$$

where the divergence in  $T_n^\pm$  is given by

$$(\rho_n^\pm)^{-2} \frac{\partial [\pm (\rho_n^\pm)^2 \mathbf{f}_n]}{\partial \rho_n^\pm} \quad (\text{A.24})$$

$$\nabla \cdot \mathbf{J}(\mathbf{r}) = -j\omega\rho(\mathbf{r}) \quad (\text{A.25})$$

The charge density is proportional to  $\nabla \cdot \mathbf{f}_n$  through (A.25), (2.16) and (A.22) is constant within each tetrahedron.

5) The moment of  $\mathbf{f}_n$  over  $T_n^\pm$  is

$$\int_{T_n^\pm} \mathbf{f}_n d\mathbf{v} = \frac{a_n}{3} \rho_n^{c\pm} \quad (\text{A.26})$$

where  $\rho_n^{c\pm}$  is the vector between the free vertex and the centroid of  $T_n^\pm$  with  $\rho_n^{c-}$  directed toward and  $\rho_n^{c+}$  directed away from the vertex. (A.26) may be most easily derived by expressing the integral in terms of volume coordinates.

6) If face  $n$  is on the boundary of  $V$ , then only one of the tetrahedrons,  $T_n^+$  or  $T_n^-$ , is interior to  $V$ . In this case it is assumed that  $\mathbf{f}_n$ , is defined only over the interior tetrahedron and that the exterior tetrahedron is not defined.

Some of the less obvious of these properties can be verified. An important interpretation of (A.22) that follows from 1) and 3) is that the expansion coefficient  $D_n$ , represents the normal component of  $\mathbf{D}(\mathbf{r})$  at the  $n$ th face.

The modeling properties of the basis functions  $\mathbf{f}_n$  are similar to those of the rooftop functions that are used to model surface current distributions. Property 1) guarantees that the expansion (A.22) can provide at least a piecewise constant approximation to the flux density. Furthermore, each function varies linearly with distance from its defining vertex. This provides some capability to model linear field variations. However, like the rooftop functions, these basis functions are constant in the transverse direction so they cannot accurately represent a vector field with arbitrary linear

variation; they can reproduce linear variations of the field only if the variation is parallel to the direction of the field defined by the basis function. In order to solve (2.15) with  $\mathbf{D}(\mathbf{r})$  represented by (A.2), it is necessary to find expressions for  $\mathbf{J}(\mathbf{r})$  and  $\rho(\mathbf{r})$  in terms of the basis functions and expansion coefficients. From (A.22) and (2.16)

$$\mathbf{J}(\mathbf{r}) = j\omega \sum_{n=1}^N D_n \kappa(\mathbf{r}) \mathbf{f}_n(\mathbf{r}) \quad (\text{A.27})$$

In (A.27), the parameter  $\kappa(\mathbf{r})$  is taken inside the summation to emphasize that the polarization or contrast current at each point in the body is a weighted sum of the basis functions at that point times a factor that describes the medium at that point. By substituting (A.27) into (A.25) and using (A.23), the charge density is found to be represented by

$$\rho(\mathbf{r}) = - \sum_{n=1}^N D_n \kappa(\mathbf{r}) \nabla \cdot \mathbf{f}_n(\mathbf{r}) - \sum_{n=1}^N D_n \mathbf{f}_n(\mathbf{r}) \cdot \nabla \kappa(\mathbf{r}) \quad (\text{A.28})$$

The first summation is the induced volume charge densities  $\rho_{vn}$  associated with the basis functions and can be evaluated with the aid of (A.23)

$$\rho_{vn}(\mathbf{r}) = \begin{cases} -D_n \kappa_n^+ \frac{a_n}{V_n^+}, & \mathbf{r} \in T_n^- \\ D_n \kappa_n^- \frac{a_n}{V_n^-}, & \mathbf{r} \in T_n^+ \\ 0, & \text{otherwise} \end{cases} \quad (\text{A.29})$$

where  $\kappa_n^\pm$  is the constant value of  $\kappa(\mathbf{r})$  in  $T_n^\pm$ . The second summation in (A.28) represents the induced surface charge densities associated with the basis functions. When the  $n$ th face separates dissimilar media,  $\kappa$  is discontinuous and its gradient is a generalized function representing a surface charge density  $\rho_{sn}$ , residing on  $a_n$ ,

$$\rho_{sn}(\mathbf{r}) = \begin{cases} D_n (\kappa_n^+ - \kappa_n^-), & \mathbf{r} \in a_n \\ 0, & \text{otherwise} \end{cases} \quad (\text{A.30})$$

An induced volume charge associated with each basis function exists in each tetrahedron for which the medium parameters differ from those of free space. It can be shown that the formulation of the problem in (2.11, 2.13, 2.14, 2.15, A.25) guarantees that the total volume charge in a homogeneous region is zero. In the numerical procedure, the total volume charge, which is the sum of the volume charges associated with the four basis functions in each tetrahedron, is not explicitly constrained to be zero, but should be small for any solution that is close to the true solution. An induced surface charge exists only on faces that separate dissimilar media, and the charge density is constant on such faces. The correct surface charge representation is obtained at the faces because of the careful construction of the representation of  $\mathbf{J}$ . Equations (A.22), (A.27), and (A.28) can be used in (2.11)-(2.14) to obtain an equation involving only the unknown coefficients  $D_n$  and known vector functions.

## A.2.2 Testing Procedure of SWG Basis Function

The next step in applying the method of moments is to select a testing procedure that will generate  $N$  independent equations for the unknown expansion coefficients. The expansion functions  $f_m$

developed in the previous section are chosen as testing functions. With a symmetric product defined as

$$\langle \mathbf{f}, \mathbf{g} \rangle \equiv \int_V \mathbf{f} \cdot \mathbf{g} dv \quad (\text{A.31})$$

(2.15) is tested with  $\mathbf{f}_m$ , yielding

$$\langle \mathbf{D}/\hat{\epsilon}, \mathbf{f}_m \rangle + j\omega \langle \mathbf{A}, \mathbf{f}_m \rangle + \langle \nabla \Phi, \mathbf{f}_m \rangle = \langle \mathbf{E}^{inc}, \mathbf{f}_m \rangle, \quad m = 1, 2, \dots, N. \quad (\text{A.32})$$

This represents  $N$  equations for the  $N$  unknown coefficients  $\{D_n\}$  and can be written in matrix form as

$$[S_{mn}][D_n] = [E_m] \quad (\text{A.33})$$

where  $[S_{mn}]$  is an  $N \times N$  matrix with dimensions of  $m^4/F$ , and  $[D_n]$  and  $[E_m]$  are column vectors of length  $N$ . Since the elements of  $[S_{mn}]$  and  $[E_m]$  cannot be evaluated in closed form, it is necessary to derive accurate and efficient numerical approximations for these quantities. Formulas for the matrix (A.33) elements and some considerations relevant to their computation are given in the next section

### A.2.3 Elements of the Matrix and Excitation Vector of SWG

The formulas that are used to fill the matrix  $[S_{mn}]$  and the excitation vector  $[E_m]$  are derived from (A.32) as follows. The first term of (A.32) can be written as

$$\begin{aligned} \langle \mathbf{D}/\hat{\epsilon}, \mathbf{f}_m \rangle &= \sum_{n=1}^N D_n \langle \mathbf{f}_n/\hat{\epsilon} \rangle \\ &= \sum_{n=1}^N D_n \left[ \frac{1}{\hat{\epsilon}_n^+} \int_{T_m^+} \mathbf{f}_n \cdot \mathbf{f}_m dv + \frac{1}{\hat{\epsilon}_n^-} \int_{T_m^-} \mathbf{f}_n \cdot \mathbf{f}_m dv \right] \end{aligned} \quad (\text{A.34})$$

(Recall that  $\mathbf{f}_m$  is zero outside of  $T_m^\pm$ ) These integrals can be evaluated by utilizing normalized volume coordinates. By using the volume coordinate representation of the basis functions and formulas for integration in volume coordinates, the integral of  $\mathbf{f}_i \cdot \mathbf{f}_j$  over  $T^p$  can be evaluated as

$$\begin{aligned} \int_{T^p} \mathbf{f}_i \cdot \mathbf{f}_j dv &= \frac{a_i a_j}{9V^p} \left[ \frac{8}{5} |\mathbf{r}^{cp}|^2 - (\mathbf{r}_i + \mathbf{r}_j) \cdot \mathbf{r}^{cp} + (\mathbf{r}_i \cdot \mathbf{r}_j) \right. \\ &\quad \left. - \frac{1}{10} (\mathbf{r}_1 \cdot \mathbf{r}_2 + \mathbf{r}_1 \cdot \mathbf{r}_3 + \mathbf{r}_1 \cdot \mathbf{r}_4 + \mathbf{r}_2 \cdot \mathbf{r}_3 + \mathbf{r}_2 \cdot \mathbf{r}_4 + \mathbf{r}_3 \cdot \mathbf{r}_4) \right] \end{aligned} \quad (\text{A.35})$$

where  $\mathbf{r}_{cp}$  is the vector from  $O$  to the centroid of  $T_p$  and  $\mathbf{r}_1, \mathbf{r}_2, \mathbf{r}_3, \mathbf{r}_4$  are vectors from  $O$  to the vertices of  $T$ . This result can be used to complete the evaluation of (A.34). The second term and the right side of (A.32) both involve an integration over a vector field, and they can be treated similarly. In particular,  $\mathbf{A}$  and  $\mathbf{E}^{inc}$  are assumed to vary slowly enough to be approximated within each tetrahedron by their values at the centroid of the tetrahedron. Then, by (A.26),

$$\left\langle \begin{pmatrix} \mathbf{A} \\ \mathbf{E}^{inc} \end{pmatrix}, \mathbf{f}_m \right\rangle \approx \begin{pmatrix} \mathbf{A}(\mathbf{r}_m^{c+}) \\ \mathbf{E}^{inc}(\mathbf{r}_m^{c+}) \end{pmatrix} \cdot \frac{a_m \rho_m^{c+}}{3} + \begin{pmatrix} \mathbf{A}(\mathbf{r}_m^{c-}) \\ \mathbf{E}^{inc}(\mathbf{r}_m^{c-}) \end{pmatrix} \cdot \frac{a_m \rho_m^{c-}}{3} \quad (\text{A.36})$$

If  $T_m^+$  or  $T_m^-$  is not in  $V$ , then the corresponding term is absent in (A.36). In (A.36),  $\mathbf{r}_m^{c\pm}$  is the vector from  $O$  to the centroid of  $T_m^\pm$  and  $\rho_m^{c\pm}$  is the vector from the vertex opposite  $a_m$  in  $T_m^\pm$  to the centroid of  $T_m$ .

The scalar potential term of (A.32) can be written as

$$\langle \nabla \Phi, \mathbf{f}_m \rangle = \int_S \Phi \mathbf{f}_m \cdot \hat{\mathbf{n}} ds - \int_V \Phi \nabla \cdot \mathbf{f}_m dv \quad (\text{A.37})$$

where  $S$  is the boundary of  $V$ . Since the tangential component of  $\mathbf{f}_m$ , is discontinuous at tetrahedral boundaries, verification of (A.37) requires that the contributions from individual tetrahedral volume elements and their boundaries be summed. This leads directly to the last term of (A.37). The surface integral follows from the fact that the normal component of  $\mathbf{f}_m$ , is continuous or vanishes at all boundaries internal to  $V$ . Then, with the assumption that  $\Phi$  is sufficiently slowly varying that it may be replaced by its value at the centroid of a tetrahedron or face, (A.37) becomes

$$\langle \nabla \Phi, \mathbf{f}_m \rangle = \begin{cases} a_m [\Phi(\mathbf{r}_m^{c-}) - \Phi(\mathbf{r}_m^{c+})], & T_m^+ \text{ and } T_m^- \text{ in } V \\ \pm a_m [\Phi(\mathbf{r}_m^{c\pm} \pm 1/3 \rho_m^{c\pm}) - \Phi(\mathbf{r}_m^{c\pm})], & T_m^\pm \text{ not in } V \end{cases} \quad (\text{A.38})$$

The argument  $(\mathbf{r}_m^{c\pm} \pm 1/3 \rho_m^{c\pm})$  denotes that  $\Phi$  is evaluated at the centroid of face  $m$  when  $T_m^\pm$  is not in  $V$ . When the elements of  $[S_{mn}]$  are calculated, the contributions to  $\mathbf{A}$  and  $\Phi$  from a single basis function are needed. These are given by

$$\mathbf{A}_n(r) = \frac{\mu_0 a_n}{12\pi} \left[ \frac{\kappa_n^+}{V_n^+} \int_{T_n^+} \rho_n^+ \frac{e^{-jkR}}{R} dv' + \frac{\kappa_n^-}{V_n^-} \int_{T_n^-} \rho_n^- \frac{e^{-jkR}}{R} dv' \right] \quad (\text{A.39})$$

$$\Phi_n(r) = \frac{-a_n}{j\omega 4\pi \epsilon_0} \left[ \frac{\kappa_n^+}{V_n^+} \int_{T_n^+} \frac{e^{-jkR}}{R} dv' - \frac{\kappa_n^-}{V_n^-} \int_{T_n^-} \frac{e^{-jkR}}{R} dv' - \frac{(\kappa_n^+ - \kappa_n^-)}{a_n} \int_{a_n} \frac{e^{-jkR}}{R} ds' \right] \quad (\text{A.40})$$

where  $\kappa_n^\pm$  is taken to be zero if  $T_n^\pm$  is not in  $V$ .

By expressing them in terms of normalized volume coordinates, the integrals in (A.39) and (A.40) may be readily evaluated numerically. They can, in fact, be expressed in terms of four independent scalar integrals over each tetrahedron. These four integrals contribute to 16 different elements of  $[S_{mn}]$ . Considerable savings in computation time is achieved by making use of these multiple contributions.

# Bibliography

- [1] V.G.Veselago, “The electrodynamics of substances with simultaneously negative values of  $\varepsilon$  and  $\mu$ ,” *spu*, vol. 10, no. 4, pp. 509–514, Jan 1968.
- [2] J. B. Pendry, A. J. Holden, and W. J. S. D. J. Robbins, “Magnetism from conductors and enhanced nonlinear phenomena,” *IEEE Trans. Microwave Theory Tech.*, vol. 47, no. 11, pp. 2075 – 2084, Nov 1999.
- [3] D. R. Smith and D. Schurig, “Electromagnetic wave propagation in media with indefinite permittivity and permeability tensors,” *Phys. Rev. Lett.*, vol. 90, no. 7, p. 077405, Feb 2003.
- [4] J. B. Pendry, “Negative refraction makes a perfect lens,” *Phys. Rev. Lett.*, vol. 85, no. 18, pp. 3966–3969, Oct 2000.
- [5] R. A. Shelby, D. R. Smith, S. C. Nemat-Nasser, and S. Schultz, “Microwave transmission through a two-dimensional, isotropic, left-handed metamaterial,” *Appl. Phys. Lett.*, vol. 78, pp. 489–491, Jan 2001.
- [6] K. Li, S. J. McLean, R. B. Greegor, C. G. Parazzoli, and M. H. Tanielian, “Free-space focused-beam characterization of left-handed materials,” *Appl. Phys. Lett.*, vol. 82, pp. 2535–2537, Apr 2003.
- [7] R. A. Shelby, D. R. Smith, and S. Schultz, “Experimental verification of a negative index of refraction,” vol. 292, pp. 77–79, Apr 2001.
- [8] A. A. Houck, J. B. Brock, and I. L. Chuang, “Experimental observations of a left-handed material that obeys snell’s law,” *Phys. Rev. Lett.*, vol. 90, p. 137401, Apr 2003.
- [9] P. Markoš and C. M. Soukoulis, “Numerical studies of left-handed materials and arrays of split ring resonators,” *Phys. Rev. E*, vol. 65, p. 045601, Mar 2002.
- [10] I. R. P. Markoš and C. M. Soukoulis, “Transmission losses in left-handed materials,” *Phys. Rev. E*, vol. 66, p. 045601, Oct 2002.
- [11] J. P. Jr., T. M. G. B.-I. W. Y. Zhang, and J. A. Kong, “Power propagation in homogeneous isotropic frequency-dispersive left-handed media,” *Phys. Rev. Lett.*, vol. 89, p. 257401, Dec 2004.
- [12] P. Markoš and C. M. Soukoulis, “Absorption losses in periodic arrays of thin metallic wires,” *Optics Lett.*, vol. 28, no. 10, 2003.

- [13] T. Koschny, P. Markoš, D. R. Smith, and C. M. Soukoulis, “Resonant and antiresonant frequency dependence of the effective parameters of metamaterials,” *Phys. Rev. E*, vol. 68, p. 065602, Dec 2003.
- [14] N. Katsarakis, T. Koschny, M. Kafesaki, E. N. Economou, and C. M. Soukoulis, “Electric coupling to the magnetic resonance of split ring resonators,” *Appl. Phys. Lett.*, vol. 84, no. 15, pp. 2943–2945, Apr 2004.
- [15] H. Chen, L. Ran, J. Huangfu, X. Zhang, K. Chen, T. M. Grzegorzczuk, and J. A. Kong, “T-junction waveguide experiment to characterize left-handed properties of metamaterials,” *jap*, vol. 94, no. 3712, pp. 3712–3716, Sep 2003.
- [16] T. Weiland, R. Schuhmann, R. B. Greger, C. G. Parazzoli, A. M. Vetter, D. R. Smith, D. C. Vier, and S. Schultz, “Ab initio numerical simulation of left-handed metamaterials: Comparison of calculations and experiments,” *jap*, vol. 90, no. 10, pp. 5419–5424, Nov 2001.
- [17] P. Gay-Balmaz and O. J. F. Martin, “Electromagnetic resonances in individual and coupled split-ring resonators,” *J. Appl. Phys.*, vol. 92, no. 5, pp. 2929–2936, Sep 2002.
- [18] H.-Y. Yao, L.-W. Li, Q. Wu, and J. A. Kong, “Macroscopic performance analysis of metamaterials synthesized from microscopic 2-d isotropic cross split-ring resonator array,” *Progress In Electromagnetics Research*, vol. 51, pp. 197–217, 2005.
- [19] A. Sanada., C. Caloz, and T. Itoh, “Characteristics of the composite right/left-handed transmission lines,” *IEEE Microwave Wireless Compon. Lett.*, vol. 14, no. 2, pp. 68–70, Feb 2004.
- [20] G. V. Eleftheriades, A. K. Iyer, and P. C. Kremer, “Planar negative refractive index media using periodically l-c loaded transmission lines,” *IEEE Trans. Microwave Theory Tech.*, vol. 50, no. 12, pp. 2702 – 2712, Dec 2002.
- [21] W.-B. Ewe, L.-W. Li, and M.-S. Leong, “Fast solution of mixed dielectric/conducting scattering problem using volume-surface adaptive integral method,” *IEEE Trans. Antennas Propagat.*, vol. 52, no. 11, pp. 3071–3077, Nov 2004.
- [22] R. F. Harrington, *Field Computation by Moment Method*, 1st ed. New York: The Macmillan Company, 1968.
- [23] M. J. T. Bleszynski, E.; Bleszynski, “Aim: Adaptive integral method for solving large-scale electromagnetic scattering and radiation problems,” *Radio Sci.*, vol. 31, no. 5, pp. 1225–1252, 1996.
- [24] M. Bleszynski, E. and Bleszynski and T. Jaroszewicz, “A fast integral-equation solver for electromagnetic scattering problems,” *IEEE APS Int. Symp. Dig.*, pp. 416 – 419, Jun 1994.
- [25] D. H. Preis, “The toeplitz matrix: Its occurrence in antenna problems and a rapid inversion algorithm,” *IEEE Trans. Antennas Propagat.*, vol. 20, no. 2, pp. 204–206, Mar 1972.
- [26] W. Rotman, “Plasma simulation by artificial dielectrics and parallel-plate media,” *IEEE Trans. Antennas Propagat.*, vol. 10, no. 1, pp. 82 – 95, Jan 1962.

- [27] J. B. Pendry, A. J. Holden, D. J. Robbins, and W. J. Stewart, “Low frequency plasmons in thin-wire structures,” *J. Phys.: Condens. Matter*, vol. 10, p. 4785C4809, 1998.
- [28] D. R. Smith, W. J. Padilla, D. C. Vier, S. C. Nemat-Nasser, and S. Schultz, “Composite medium with simultaneously negative permeability and permittivity,” *Phys. Rev. Lett.*, vol. 84, no. 18, pp. 4184–4187, May 2000.
- [29] C. D. Moss, T. M. Grzegorzczak, Y. Zhang, and J. A. Kong, “Numerical studies of left handed metamaterials,” *Progress In Electromagnetics Research*, vol. 35, pp. 315–334, 2002.
- [30] V. Rokhlin, “Rapid solution of integral equations of scattering theory in two dimensions,” *J. Comput. Phys.*, vol. 86, no. 2, pp. 414–439, Feb 1990.
- [31] R. Coifman, V. Rokhlin, and S. Wandzura, “The fast multipole method for the wave equation: a pedestrian prescription,” *IEEE Trans. Antennas Propagat.*, vol. 35, no. 3, pp. 7–12, Jun 1993.
- [32] J. Song, C.-C. Lu, and W. C. Chew, “Multilevel fast multipole algorithm for electromagnetic scattering by large complex objects,” *IEEE Trans. Antennas Propagat.*, vol. 45, no. 10, pp. 1488 – 1493, Oct 1997.
- [33] T. K. Sarkar, E. Arvas, and S. M. Rao, “Application of fft and the conjugate gradient method for the solution of electromagnetic radiation from electrically large and small conducting bodies,” *IEEE Trans. Antennas Propagat.*, vol. 34, no. 5, pp. 635–640, May 1986.
- [34] F. Ling, C.-F. Wang, and J.-M. Jin, “An efficient algorithm for analyzing large-scale microstrip structures using adaptive integral method combined with discrete complex-image method,” *IEEE Trans. Microwave Theory Tech.*, vol. 48, no. 5, pp. 832–839, May 2000.
- [35] Z. Q. Zhang and Q. H. Liu, “A volume adaptive integral method (vaim) for 3-d inhomogeneous objects,” vol. 1, no. 1, pp. 102–105, 2002.
- [36] Y. Chang and R. F. Harrington, “A surface formulation for characteristic modes of material bodies,” *IEEE Trans. Antennas Propagat.*, vol. 25, no. 6, pp. 789–795, Nov 1977.
- [37] L. N. Medgyesi-Mitschang and J. M. Putnam, “Electromagnetic scattering from axially inhomogeneous bodies of revolution,” *IEEE Trans. Antennas Propagat.*, vol. 32, no. 8, pp. 797 – 806, Aug 1984.
- [38] C. C. Lu and W. C. Chew, “A coupled surface-volume integral equation approach for the calculation of electromagnetic scattering from composite metallic and material targets,” *IEEE Trans. Antennas Propagat.*, vol. 48, no. 12, pp. 1866 – 1868, Dec 2000.
- [39] S. M. Rao, D. R. Wilton, and A. W. Gilsson, “Electromagnetic scattering by surfaces of arbitrary shape,” *IEEE Trans. Antennas Propagat.*, vol. 30, no. 3, pp. 409–418, May 1982.
- [40] D. H. Schaubert, D. R. Wilton, and A. W. Gilsson, “A tetrahedral modeling method for electromagnetic scattering by arbitrarily shaped inhomogeneous dielectric bodies,” *IEEE Trans. Antennas Propagat.*, vol. 32, no. 1, pp. 77–85, Jan 1984.
- [41] W.-B. Ewe, L.-W. Li, Q. Wu, and M.-S. Leong, “Preconditioners for adaptive integral method implementation,” *IEEE Trans. Antennas Propagat.*, vol. 53, no. 7, pp. 2346–2350, Jul 2005.



- [42] F. Ling, C.-F. Wang, and J.-M. Jin, "Application of adaptive integral method to scattering and radiation analysis of arbitrarily shaped planar structures," *IEEE APS Int. Symp. Dig.*, vol. 3, pp. 1778–1781, Jun 1998.
- [43] F. Falcone, T. Lopetegi, J. Baena, R. M. F. Martn, and M. Sorolla, "Effective negative- $\epsilon$  stop-band microstrip lines based on complementary split ring resonators," *IEEE Microwave Wireless Compon. Lett.*, vol. 14, pp. 280–282, 2004.
- [44] F. Falcone, T. Lopetegi, M. Laso, J. Baena, F. M. J. Bonache, R. Marqu  s, and M. Sorolla, "Babinet principle applied to the design of metasurfaces and metamaterials," *Phys. Rev. Lett.*, vol. 93, pp. 280–282, 2004.
- [45] J. Baena, F. M. J. Bonache, R. Marqu  s, F. Falcone, T. Lopetegi, M. Laso, J. Garc  a, I. Gil, and M. Sorolla, "Equivalent circuit models for split ring resonators and complementary split rings resonators coupled to planar transmission lines," *IEEE Trans. Microwave Theory Tech.*, vol. 53, pp. 1451–1461, 2005.
- [46] I. Gil, J. Bonache, M. Gil, J. Garc  a-Garc  a, and F. Mart  n, "Left-handed and right-handed transmission properties of microstrip lines loaded with complementary split rings resonators," *IEEE Microwave Wireless ComponLett.*, vol. 48, 2006.
- [47] N. Matsunaga, A. Sanada, and H. KUBO, "Novel two-dimensional planar negative refractive index structure," vol. E89-C, 2005.
- [48] F. Ling, J. Liu, and J.-M. Jin, "Efficient electromagnetic modeling of three-dimensional multilayer microstrip antennas and circuits," *IEEE Trans. Microwave Theory Tech.*, vol. 50, 2002.
- [49] N. Das and D. Pozar, "A generalized spectral-domain green's function for multilayer dielectric substrates with application to multilayer transmission lines," *IEEE Trans. Microwave Theory Tech.*, vol. 35, 1987.
- [50] L. Liu, C. Caloz, C.-C. Chang, and T. Itoh, "Forward coupling phenomena between artificial left-handed transmission lines," *J. Appl. Phys.*, vol. 92, 2002.
- [51] C.-J. Lee, K. M. K. H. Leong, and T. Itoh, "Composite right/left-handed transmission line based compact resonant antennas for rf module integration," *IEEE Trans. Microwave Theory Tech.*, vol. 54, no. 8, pp. 2283 – 2291, Aug 2006.